PHYSICAL REVIEW B **76**, 125412 (2007)

Self-similarity during growth of the Au/TiO$_2$(110) model catalyst as seen by the scattering of x-rays at grazing-angle incidence

Rémi Lazzari,[1,*] Gilles Renaud,[2,†] Jacques Jupille,[1,‡] and Frédéric Leroy[3,§]
[1]*Institut des NanoSciences de Paris, Universités Pierre et Marie Curie (Paris 6) et Denis Diderot (Paris 7), CNRS UMR 7588 Campus Boucicaut, 140 Rue de Lourmel, 75015 Paris, France*
[2]*Nanostructures et Rayonnement Synchrotron, Service de Physique des Matériaux et Microstructures, Département de Recherche Fondamentale sur la Matière Condensée, Commissariat à l'Energie Atomique, 17 Avenue des Martyrs, F-38054 Grenoble, Cedex 9, France*
[3]*Centre de Recherche en Matière Condensée et NanoSciences, CNRS-UPR 7281, Campus de Luminy Case 913, 13288 Marseille Cedex 09, France*

(Received 15 September 2006; revised manuscript received 21 May 2007; published 11 September 2007)

The growth of gold nanoparticles on TiO$_2$(110) was investigated in situ by grazing incidence x-ray scattering techniques. The in-plane diffraction showed complex epitaxial relationships with a preferential alignment of dense gold direction along the bridging oxygen rows of TiO$_2$(110) ($[1\bar{1}0]_{\mathrm{Au}} \| [001]_{\mathrm{TiO}_2}$) with a low lattice mismatch. Whatever the growth temperature ($T=300,600$ K), two nearly equiproportional epitaxial planes, i.e., $(111)_{\mathrm{Au}} \| (110)_{\mathrm{TiO}_2}$ and $(11\bar{2})_{\mathrm{Au}} \| (110)_{\mathrm{TiO}_2}$, were observed. The small angle scattering from the nanoparticles was analyzed using a truncated sphere shape with models [R. Lazzari, F. Leroy, and G. Renaud, Phys. Rev. B **76**, 125411 (2007)] that account for (i) multiple scattering effects due to the graded profile of refraction index in the normal direction and (ii) the correlation between the particle spacing and sizes. At the beginning of the growth, gold particles are pinned on defects and grow through a diffusion-limited mechanism. However, coalescence does not occur via a static mechanism. It rather involves surface diffusion of clusters. It proceeds through a self-similar mechanism, not only on the size distribution but also on the spatial ordering. Particle locations, which are no longer controlled by the randomness of nucleation centers, become dominated by the correlation between the particle size and its influence area. A strong link between island height and radius indicates that particles are close to equilibrium. Indeed, the value derived for contact angle (adhesion energy) compares well with tabulated data. In addition, the cluster size before the onset of coalescence compares with that of the gold particles at the maximum of catalytic activity for the oxidation of CO.

DOI: 10.1103/PhysRevB.76.125412 PACS number(s): 61.10.Dp, 61.10.Kw, 81.15.Aa, 68.55.Ac

I. INTRODUCTION

Recently, catalysts made of gold nanoparticles[2] have attracted the interest of numerous scientists because of their potential applications to many reactions of industrial and environmental importance. Gold catalysts are extraordinary active for the oxidation of CO at room temperature and by far more active than other noble metals below 400 K. The titania support is the warhorse of numerous fundamental studies aimed at understanding the catalytic mechanisms and at elucidating the origin of this surprising reactivity as neither titania nor bulk gold alone is active. Because the cluster morphology seems a key parameter in the understanding of the catalytic activity of gold,[3] many studies were performed by using vacuum techniques on planar TiO$_2$(110) substrate (see Refs. 4 and 5). The growth of gold on titania was characterized by microscopy techniques (scanning tunneling microscopy,[6–16] high resolution scanning electron microscopy and transmission electron microscopy[17,18]) and low-energy ion scattering.[19–21] At low coverage [0.1 ML (monolayer)], the gold clusters grow as quasi-two-dimensional particles of one or two atomic layers high, with diameters between 1 and 2 nm, which appear to be the most catalytically active maybe because of their peculiar electronic properties.[6] For higher coverages (>0.2 ML), they are rapidly mixed with hemispherical three-dimensional (3D) particles with a diameter in the range 2.5–4 nm. The biggest particles (diameter larger than 4 nm) have a higher contact angle ($\theta_c \simeq 122°$).

Pending questions are (i) the role of the crystallographic orientations of the particles,[18] (ii) the interaction between gold islands during the growth and coalescence, and (iii) the dominant mechanism (ripening or coalescence) of late stage growth on surfaces. Indeed, the clusters are believed to nucleate preferentially at defects, mainly on oxygen vacancies of bridging oxygen rows of TiO$_2$(110) or along step edges,[22–27] but it is argued that the gold clusters are not pinned on the surface and that the complex formed by gold atoms and vacancies is a diffusing entity.[12,26,27] The present study aims at giving a general picture of epitaxy, growth, and coalescence of supported particles of gold on TiO$_2$(110), as investigated by *in situ* grazing incidence in-plane x-ray diffraction (GIXD) and grazing incidence small-angle x-ray scattering (GISAXS). Using approaches which are developed in detail in Ref. 1 and briefly sketched in Sec. II, two important effects that were neglected up to that point in the GISAXS data analysis will be taken into account: (i) the multiple scattering from the graded interface in the normal direction and (ii) the link between size and spacing of the particles in the in-plane direction. The morphological parameters of the particles are determined *in situ*, as well as their degree of spatial organization that seems intimately linked to them. After the description of the experimental details (Sec. II), the in-plane epitaxy (Sec. III) of the interface is explored at the first stages of the growth. The analysis of the GISAXS patterns (Sec. IV) allows us to discuss (Sec. V) several characteristics of the particle growth: (i) the growth laws, i.e., the

1098-0121/2007/76(12)/125412(18)

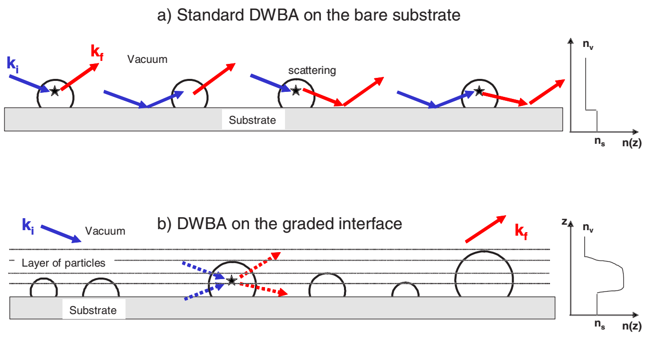

FIG. 1. (Color online) The scattering $\mathbf{k_i} \rightarrow \mathbf{k_f}$ from one island along the perpendicular direction can be treated in DWBA using as an unperturbed state: (a) the bare substrate or (b) the graded interface and its full profile of refraction index $n(z)$. In case (a), the particle form factor includes the reflection effect of the incident and scattered on the substrate surface alone as if the particle was isolated. In case (b), the scattering is from an upward or downward to an upward or downward propagating waves inside the particle layer.

evolution of the mean morphological parameters with evaporation time; (ii) the self-similar behavior of the coalescence process, i.e., the invariance of the cluster size distributions and of the fluctuations of particle spacing upon rescaling by the mean values at different times; and (iii) the particle equilibrium shape in connection with the interface adhesion energy and the behavior under annealing.

II. GRAZING INCIDENCE X-RAY SCATTERING: ANALYSIS MODELS AND EXPERIMENTAL SETUP

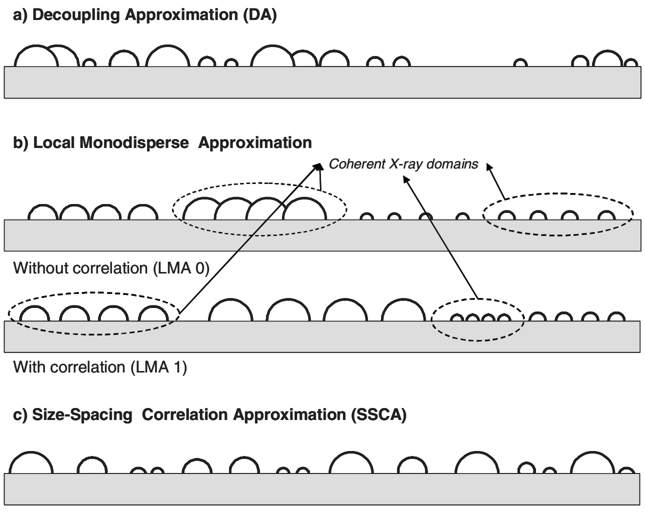

FIG. 2. Schematics of the morphology corresponding to the various approximations used to calculate x-ray diffuse scattering. Particles are placed following (a) a full disorder without any correlations (DA), (b) sets of monodisperse domains over a length scale larger than the x-ray coherence length (LMA) without correlation between size and spacing (LMA 0) or with such a correlation (LMA 1), and (c) a correlation between particle separation and their respective sizes (SSCA).

The analysis of grazing incidence diffuse scattering from a collection of nanoparticles gets more and more difficult upon increasing the surface coverage, i.e., the packing of islands. Incident and scattered waves are reflected not only at flat interfaces[28,29] but also by the particle layer itself (Fig. 1). The multiple scattering due to the grazing geometry and the full refraction index profile were recently modeled[1] via the distorted wave born approximation (DWBA).[30–32] The concept of particle form factor was generalized by including the amplitudes and wave vectors of the upward and downward propagating waves along the surface normal. It was demonstrated that both Yoneda's peak and the form factor interference fringes were strongly dependent on the profile of refraction index. Conversely, in-plane partial interference functions between particles of different sizes[33] are usually determined either by ignoring correlations [decoupling approximation[34–38] (DA)] or by modeling the scattering particles as a set of monodisperse domains [local monodisperse approximation[34,39–42] (LMA)] (Fig. 2). However, the scaling of the influence area of each supported particle with its size is a key ingredient of its growth mode[43] (Fig. 2) and gives rise to a clear signature in the scattering pattern.[44] The coupling between the particle sizes and spacings was introduced in a modified one-dimensional (1D) paracrystal[37,45–47] model called size-spacing correlation approximation (SSCA),[1] in which the distance d_n separating two neighboring particles of sizes R_{n-1} and R_n follows a Gaussian law:

$$p(d_n/[R_{n-1},R_n]) = \frac{1}{\sigma_D\sqrt{2\pi}} \exp\left[-\frac{(d_n-\langle d_n/[R_{n-1},R_n]\rangle)^2}{2\sigma_D^2}\right], \tag{2.1}$$

with a central value

$$\langle d_n/[R_{n-1},R_n]\rangle = D + \kappa[R_{n-1}+R_n-2\langle R\rangle], \tag{2.2}$$

with D being the average distance between neighboring particles, $\langle R\rangle$ the mean particle radius, κ a correlation factor, and σ_D the variance of the cumulative disorder within a paracrystal description of the lattice. The fluctuations of spacings given by $\langle (d_n-D)^2\rangle$ contain two contributions:

$$\langle (d_n-D)^2\rangle = \sigma_D^2 + 2\kappa^2\sigma_R^2. \tag{2.3}$$

The parameter σ_D^2 is intrinsic to the underlying paracrystal, while $2\kappa^2\sigma_R^2$ is linked to the fluctuations of particle sizes $[\sigma_R^2=\langle (R-\langle R\rangle)^2\rangle]$. At the limit $\kappa=0$, the DA is recovered with a 1D paracrystal interference function:[37,47]

$$S_p(q_\parallel) = \frac{1-e^{-q_\parallel^2\sigma_D^2}}{1+e^{-q_\parallel^2\sigma_D^2}-2e^{-q_\parallel^2\sigma_D^2/2}\cos(q_\parallel D)}, \tag{2.4}$$

where $q_\parallel$ is the wave vector transfer parallel to the surface.

It is important to discuss the meaning of the above 1D model and parameters in the often encountered experimental case of an isotropic two dimensional (2D) collection of particles. R_n would then be the radius of a particle labeled n, and R_{n-1} would be the average radius of its nearest neighboring particles. d_n should be interpreted as a typical size of the Voronoi cell around the particle n. d_n is chosen to depend linearly on R_n and on the average neighbor radius. Given this linear dependency [Eq. (2.2)] as already suggested in the

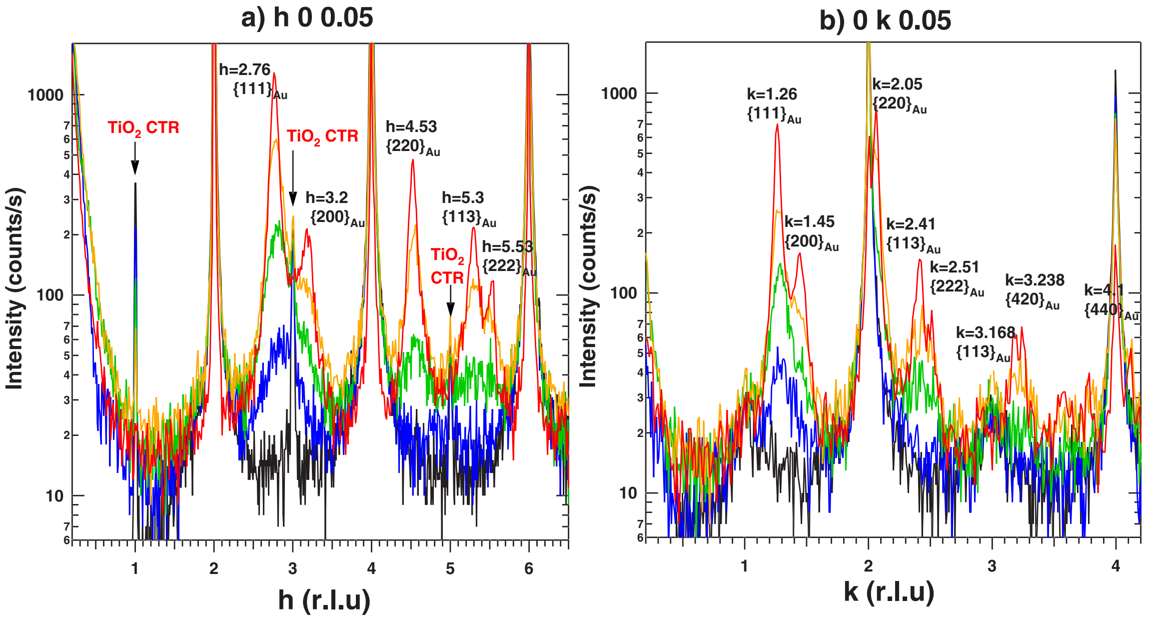

FIG. 3. (Color online) In-plane reciprocal scans as function of the amount of gold deposited at room temperature on the $TiO_2(110)$ surface. Scattered intensity versus reciprocal space coordinates in reciprocal lattice units (a) along the $(h00)$ surface direction ($[1\bar{1}0]_{TiO_2}$ bulk direction) and (b) along the $(0k0)$ surface direction ($[001]_{TiO_2}$ bulk direction). Displayed are the scans for 0 (black), 0.2 (blue), 0.8 (green), 1.6 (yellow), and 4.8 (red) nm equivalent thicknesses. The gold peaks are labeled with corresponding equivalent planes. Notice the CTR (Crystal Truncation Rod) of TiO_2 at $(n,0,0)$, $n=1,3,5$.

literature on theoretical modeling of epitaxial growth through rate equations,[48–54] Eq. (2.1) simply assumes a Gaussian distribution of Voronoi cell sizes.

The x-ray scattering experiments have been performed on the SUV (Surface sous Ultra-Vide) station[55] at the BM32 bending magnet beamline of the European Synchrotron Radiation Facility (Grenoble, France). The sample is mounted vertically on the head of a six-circle diffractometer ("z-axis type") which holds the UHV chamber (base pressure of 1×10^{-10} mbar) and allows for a precise positioning of the incoming angle α_i and of the outgoing in-plane $(2\theta_f)$ and out-of-plane (α_f) angles that are related to the x-ray wave vector transfer through[44,56]

$$q_x = k_0[\cos(\alpha_f)\cos(2\theta_f) - \cos(\alpha_i)],$$

$$q_y = k_0[\cos(\alpha_f)\sin(2\theta_f)],$$

$$q_z = k_0[\sin(\alpha_f) + \sin(\alpha_i)],$$

$$k_0 = 2\pi/\lambda. \tag{2.5}$$

The x-ray energy was set at $E=18$ keV ($\lambda=0.068\,88$ nm) (i) to avoid absorption and fluorescence by the substrate and the film and (ii) to have a good compromise on the accessible range of reciprocal space in small and wide angle scattering. The incidence was fixed at the critical angle of TiO_2 for total external reflection at the corresponding energy ($\alpha_c=0.131°$) to minimize bulk signal. The x-ray beam was sagittally focused on the sample with a horizontal $H=0.4$ mm and vertical $V=0.3$ mm sizes [full width at half maximum (FWHM)], corresponding to divergences of $\delta_H=1$ mrad and $\delta_V=0.13$ mrad, respectively.

A standard scintillator NaI detector was used for GIXD measurements. The vertical acceptance defined by slits was set to ~0.2° for the in-plane scans. A point of the reciprocal space is defined by its coordinates (h,k,ℓ) in the $(\mathbf{a}^*,\mathbf{b}^*,\mathbf{c}^*)$ basis first two components of which are linked to the surface unit cell $(\mathbf{a},\mathbf{b})$ of $TiO_2(110)$ and the third is along the surface normal $\mathbf{c}$. These components are related to the quadratic bulk unit cell of TiO_2 $(\mathbf{A},\mathbf{B},\mathbf{C})$ through $\mathbf{a}=\mathbf{A}-\mathbf{B}$, $\mathbf{b}=\mathbf{C}$, $\mathbf{c}=\mathbf{A}+\mathbf{B}$, with $a=c=\sqrt{2}A=0.6508$ nm and $b=C=0.2966$ nm. Thus, $\mathbf{b}$ is parallel to the bridging oxygen rows of the surface ($[001]_{TiO_2}$ bulk direction). With this convention, the reflection condition of the space group $P4_2/mnn$ of TiO_2 reads $h+k-l=2n$, while the $\mathbf{b}$ centering of the $(\mathbf{a},\mathbf{b},\mathbf{c})$ unit cell adds the $h+l=2n$ reflection condition. In-plane $\ell=0.05$ ($\alpha_i=\alpha_f=\alpha_c$) measurements were performed to determine the crystalline orientation of the gold islands during growth.

High quality GISAXS measurements require a background as reduced as possible. Slits that define the x-ray beam were associated with guard slits with slightly larger apertures to remove the diffuse scattering. The x-ray beam enters and exits the chamber through 0.5 mm beryllium windows; the unwanted small-angle scattering induced by the windows was suppressed inside the vacuum chamber by (i) a dedicated motorized slit just after the entrance windows and (ii) a tungsten beam stop just before the exit window. A complementary beam stop located just after the exit window allowed a complete removal of the transmitted and reflected beams the intensities of which are of several orders of magnitude larger than the diffuse scattering. The absorption and

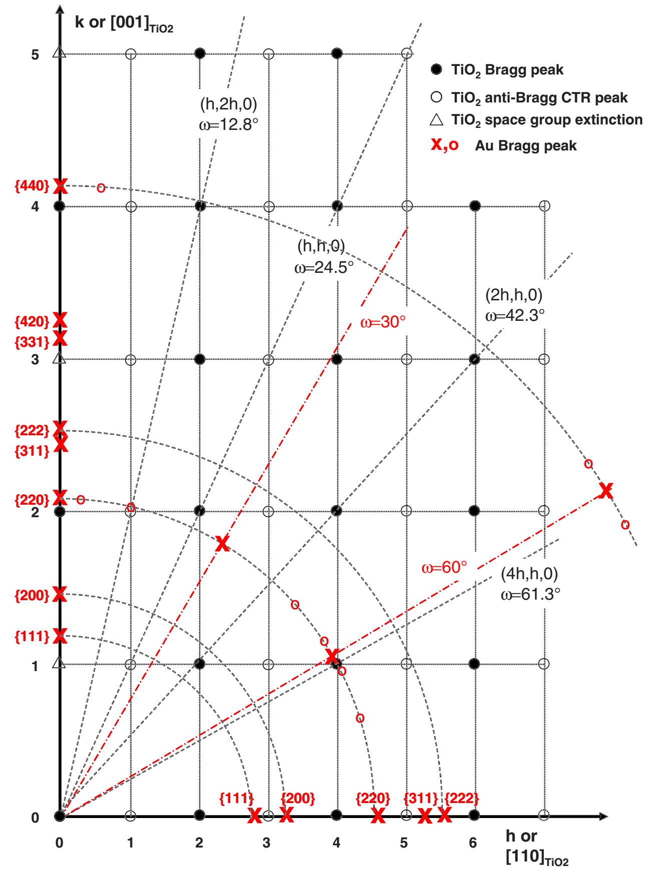

FIG. 4. (Color online) Map of the $\ell=0.05$ reciprocal space with all the observed reflections during the Au/TiO$_2$(110) growth. The $\omega=0°$ direction is $[001]_{\mathrm{TiO}_2}$.

scattering by air were avoided by setting an evacuated pipe along the beam path. The GISAXS signal was collected on a Peltier cooled 16-bit 1-Mpixel charge-coupled device camera (Princeton, Instruments, pixel size of 56.25 μm) located 0.68 m downstream the sample. Images were corrected from (i) dark counts, (ii) flat field, (iii) camera distortion, and (iv) bare substrate scattering.

The UVH chamber is equipped with an ion gun, a reflection high-energy electron diffraction setup, and an Auger electron spectrometer. High purity gold was evaporated from a cell held at $T=1500$ K. The evaporation rate (0.1 nm/min) was calibrated by both *ex situ* reflectivity on a silicon sample and a *in situ* quartz microbalance. The TiO$_2$(110) cylindrical (diameter 14 mm, thickness 1.5 mm) crystals were supplied chemomechanically polished with the lowest roughness ($R_a=0.5$ nm) and a miscut smaller than 0.1°. Three notches at 120° allowed us to clamp them with tantalum pieces on the molybdenum sample holder while leaving the surface free for x-ray grazing incidence. Samples could be annealed by electron bombardment of the molybdenum holder; the temperature was estimated by pyrometry. Before insertion in the chamber, crystals were annealed in air at $T=1200$ K to improve the crystallinity and to reduce the mosaic spread. A typical value of the rocking FWHM of the {002}-bulk Bragg reflection was $\Delta\omega_{(020)}=0.08°$. The surface was prepared *in situ* by several cycles of Ar$^+$ bombardment (1 keV, 10 μA) at 300 K followed by annealing at 1250 K and cooling down under oxygen partial pressure ($p_{O_2}=5\times10^{-5}$ mbar).[4] The main criterion for surface quality was to get the largest integrated intensity and the smallest width for the in-plane anti-Bragg reflections at equal distance between two Bragg peaks across the crystal truncation rod. The typical FWHM of 0.03°–0.1° of the (110) surface peak corresponded to a terrace width $L_\omega \simeq 2\pi/q_\parallel^{(110)}\Delta\omega^{(110)}$ of 150–500 nm.

III. COMPLEX EPITAXIAL ORIENTATION OF THE Au/TiO$_2$(110) INTERFACE

All studies of the epitaxial relationship at the Au/TiO$_2$(110) interface agree with the existence of the $(111)_{\mathrm{Au}}\|(110)_{\mathrm{TiO}_2}$ orientation.[18,19,57] A $(11\bar{2})_{\mathrm{Au}}\|(110)_{\mathrm{TiO}_2}$ orientation was obtained for samples obtained either by evaporation on hot substrates[18] or gold clusters obtained by high-energy ion implantation followed by annealing.[58] The present work focuses on the occurrence of these epitaxies at the first stages of the growth (particle radius $R<3$ nm).

In-plane $\ell\sim0.05$ (i.e., $\alpha_i=\alpha_f=\alpha_c$) scans were performed during the cumulative growth of gold islands at 300 and 600 K and for thin films deposited at 300 K followed by a flash annealing (2 min) at $T=850$ K. The two radial scans $(h,0,0.05)$ and $(0,k,0.05)$ of Fig. 3 give an overview of the observed behavior for all the growth conditions. A schematic representation of the $\ell=0.05$ reciprocal space (Fig. 4) where the deposit peaks were indexed in the reciprocal lattice of fcc gold ($a_{\mathrm{Au}}=0.407\,82$ nm) summarizes all measurements. When scanning in the $(h,0,0.05)$ direction, two main peaks show up, at $h=2.76$ for an equivalent thickness $t>0.2$ nm and at $h=4.53$ for $t>0.8$ nm. In the perpendicular direction, the main features that arise for $t>0.2$ nm are located at $k=1.26$ and $k=2.05$.

The ($h=0$, $k=2.05$) peak indicates that the dense rows of gold $[1\bar{1}0]_{\mathrm{Au}}$ are aligned with the bridging oxygen row of TiO$_2$, i.e., $[001]_{\mathrm{TiO}_2}$, a direction along which the lattice mismatch is only 2.6%. A hint about the epitaxial planes is given by the out-of-plane scan ($h=0$, $k=2.05,\ell$) of Fig. 5(b). A typical $(111)_{\mathrm{Au}}\|(110)_{\mathrm{TiO}_2}$ stacking with faults or twin islands is observed and confirmed by an azimuthal ω scan [Fig. 5(a)] with a threefold symmetry. This corresponds to a $(111)_{\mathrm{Au}}\|(110)_{\mathrm{TiO}_2}$ epitaxy with $[1\bar{1}0]_{\mathrm{Au}}\|[001]_{\mathrm{TiO}_2}$ and $[11\bar{2}]_{\mathrm{Au}}\|[1\bar{1}0]_{\mathrm{TiO}_2}$ epitaxies. However, the appearance of a $(11\bar{2})_{\mathrm{Au}}$ reflection (although bulk forbidden) at ($h=0$, $k=2.05$, $\ell=3.94$) and of a $(111)_{\mathrm{Au}}$ reflection at ($h=2.76$, $k=0$, $\ell=0.05$) and $(222)_{\mathrm{Au}}$ reflection at ($h=5.53$, $k=0$, $\ell=0.05$) point to an additional epitaxy with $(11\bar{2})_{\mathrm{Au}}\|(110)_{\mathrm{TiO}_2}$ epitaxial plane and $[1\bar{1}0]_{\mathrm{Au}}\|[001]_{\mathrm{TiO}_2}$ and $[111]_{\mathrm{Au}}\|[1\bar{1}0]_{\mathrm{TiO}_2}$ directions. As already shown by Cosandey *et al.*[18] (see Fig. 10 of this reference), the two epitaxies share the common $[1\bar{1}0]_{\mathrm{Au}}\|[001]_{\mathrm{TiO}_2}$ direction; the low lattice mismatch along this direction or an enhanced surface diffusion along the bridging oxygen rows could explain the stabilization of the high surface energy $(11\bar{2})_{\mathrm{Au}}$. A similar epitaxial behavior with the alignment of the closed packed of the

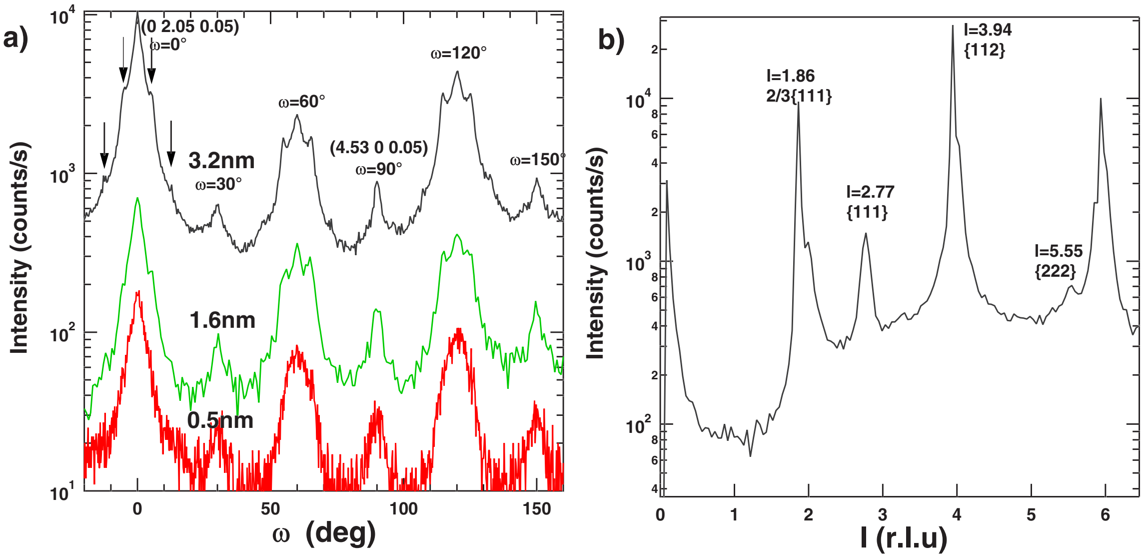

FIG. 5. (Color online) (a) ω scan or azimuthal scan at a constant wave vector transfer $q=43.5$ nm^{-1} corresponding to a {220} gold interplanar distance of $d_{\{220\}}=0.144$ nm. The film is grown at $T=600$ K (the thickness is given on the figure), while for the 3.2 nm last scan, a further annealing up to $T=790$ K was performed. The starting point $\omega=0°$ is (0, 2.05, 0.05) in reciprocal space units while $\omega=90°$ corresponds to (4.53, 0, 0.05). Notice the "pseudo threefold" symmetry. (b) l scan at constant ($h=0$, $k=2.05$) value performed on the 3.2 nm thick deposit grown at $T=600$ K. The reflections have been labeled in the fcc gold lattice.

metal $[1\bar{1}0]$ along the bridging oxygen row of TiO_2 has already been noticed for others fcc metals.[4] Twin in-plane epitaxial orientations rotated by 180°, i.e., $(111)_{Au}\|(110)_{TiO_2}$ with $[\bar{1}10]_{Au}\|[001]_{TiO_2}$ and $(11\bar{2})_{Au}\|(110)_{TiO_2}$ with $[\bar{1}10]_{Au}\|[001]_{TiO_2}$, are also found upon a 360° rocking scan.

At variance with the electron backscattering diffraction experiments,[18] which were performed on thicker films, the ratio of the $(11\bar{2})_{Au}\|(110)_{TiO_2}$ and $(111)_{Au}\|(110)_{TiO_2}$ epitaxies is 1:1 whatever the growth temperature is. This ratio is estimated by comparing the integrated intensities of the $\omega=60°$ and 120° peaks that belong only to the $(111)_{Au}\|(110)_{TiO_2}$ orientation and the $\omega=0°$ that belongs to both orientations (Fig. 5); indeed, the structure factor $F^{Au}_{(2\bar{2}0)}$ along this scan is constant. Another result is the complexity of the epitaxial relationships. A 30°-rotated $(111)_{Au}\|(110)_{TiO_2}$ orientation with $[1\bar{1}0]_{Au}\|[1\bar{1}0]_{TiO_2}$ is also observed in the azimuthal scan [Fig. 5(a)]. For $t>1.6$ nm, the two peaks ($h=3.2$, $k=0$) and ($h=0$, $k=1.45$), i.e., indexed as $\{200\}_{Au}$, correspond to a further epitaxy $(001)_{Au}\|(110)_{TiO_2}$ with $[001]_{Au}\|[001]_{TiO_2}$ as confirmed by ℓ scans (not shown). The ($h=0$, $k=1.26$) peak that corresponds to $\{111\}_{Au}$ reflection could not be assigned safely. At higher coverage, the crystallography of the interface becomes more and more complex as highlighted by the appearance of other high index reflections.

Besides the main $(111)_{Au}\|(110)_{TiO_2}$ epitaxy ($\omega=0°,60°,120°$ peaks of Fig. 5), islands rotated by $\Delta\omega=4.9°$ and $\Delta\omega=12.7°$ are evidenced (Fig. 5). Although the $\omega=12.7°$ direction is aligned with the $[1\bar{1}2]_{TiO_2}$ direction, the other does not correspond to any simple surface direction. As already seen for Pt/MgO(001),[59] a suggestion is that defined rotations of islands minimize the interfacial energy or, in other words, that the various epitaxies might correspond to intermediate minima in energy of the Au/TiO_2(110) system. To conclude, note that for the 3.2 nm thick film (Fig. 5), a Lorentzian decomposition yields a FWHM between $\Delta\omega=2°-6°$ corresponding to a coherent domain size $d_\omega=2\pi/q_\|^{(2.0500)}\Delta\omega^{(2.0500)}$ of 1.5–3 nm in agreement with the GISAXS estimate (see below).

IV. DIFFUSE SCATTERING SIGNATURE OF CORRELATIONS IN DENSE SYSTEMS OF PARTICLES: GRAZING INCIDENCE SMALL-ANGLE X-RAY SCATTERING FROM GOLD CLUSTERS ON TiO_2(110)

A. Analysis strategy of grazing incidence small-angle x-ray scattering data and results

GISAXS patterns have been recorded both during the growth of Au/TiO_2(110) nanoparticles at 300 K and after a flash annealing of such films between each deposit step (Fig. 6). They are characteristic of the Volmer-Weber three-dimensional growth mode expected from the poorly adhesive noble metal-oxide systems.[60] During the growth, the two lobes of diffuse scattering located on each side of the beam stop, the so-called correlation peaks, progressively shrink toward the origin of the reciprocal space since their separation, size, and height are inversely proportional to the average distance between clusters $\langle D\rangle$, cluster size $\langle R\rangle$, and height $\langle H\rangle$, respectively, as all these distances increase in accordance with a growth and coalescence process.

Intensity cross sections along the parallel $2\theta_f \sim q_y$ and perpendicular $\alpha_f \sim q_z$ directions are displayed in Fig. 7. As expected for vacuum measurements, the background is close to zero (less than ten counts for an acquisition time ranging

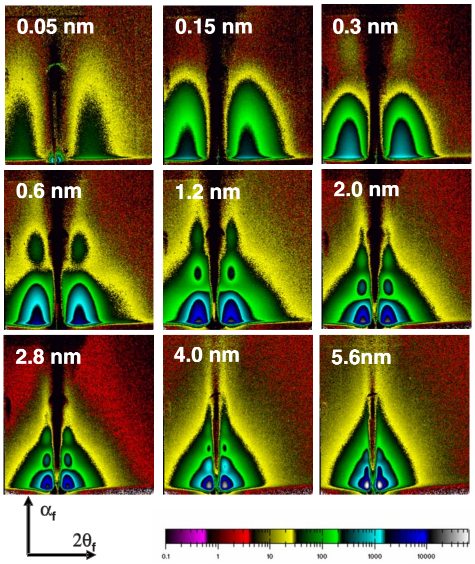

FIG. 6. (Color online) GISAXS patterns acquired *in situ* during the 3D growth of a gold film on a $TiO_2(110)$ substrate kept at room temperature. The beam was aligned along the $[1\bar{1}0]_{TiO_2}$ direction. The horizontal $2\theta_f$ (respectively, vertical α_f) axis scales to first order with the wave vector transfer $q_\parallel = q_y$ (respectively, $q_\perp = q_z$) and extends up to 3° (respectively, 3.5°). The color scale is logarithmic and the equivalent deposited thickness is given on each figure.

from 400 to 25 s).[61] The enhancement of intensity for $\alpha_f = \alpha_c$ in the perpendicular direction is usually referred to as Yoneda's peak.[62] The origin of reciprocal space is located (i) along $2\theta_f$, in the middle of the two lobes owing to the observed sample isotropy upon azimuthal rotation (Fig. 8), and (ii) along α_f, by setting the Yoneda's peak at the substrate α_c value at the early beginning of the growth, as given by the transmission function $T(\alpha_f)$ inside TiO_2 (dotted line in Fig. 7). At that stage, gold clusters produce so little roughness that $T(\alpha_f)$ should reproduce the experimental profile;[63] the only discrepancy with the 0.05 nm curve is a wider FWHM (factor of 2) that gives an upper bound of 0.05° for the instrument-induced broadening along α_f. This corresponds to the horizontal convergence of the incident beam. Upon increasing coverage, (i) interference fringes appear in the perpendicular direction (0.6 nm) up to show three bounces (Fig. 6) and (ii) the Yoneda's peak becomes round and shifts from the critical angle α_c of TiO_2 (0.1311°) to a value close to α_c of gold (0.2528°) (inset of Fig. 7). Shift and rounding cannot be accounted for by the standard DWBA the refraction effect of which only comes from the substrate.[1] In the parallel direction, the in-plane correlation peaks are clearly separated from the specular rod. As previously suggested,[44] the analysis of such a profile is not tractable within the DA[34–38] as neglecting all correlations leads to a too intense incoherent diffuse scattering for size distributed island collections. The LMA[34,39–42] would better fit the result, but it assumes scattering by independent monodisperse domains, an unphysical hypothesis in the present context. In an attempt to overcome these difficulties, the analysis of the data has been performed through the DWBA on the graded interface and the SSCA model.[1]

GISAXS patterns were nearly independent of azimuthal rotation (Fig. 8). Thus, the analysis was limited to data collected with the x-ray beam aligned along the $[1\bar{1}0]_{TiO_2}$ direction. The sensitivity to the particle shape is found in the high-

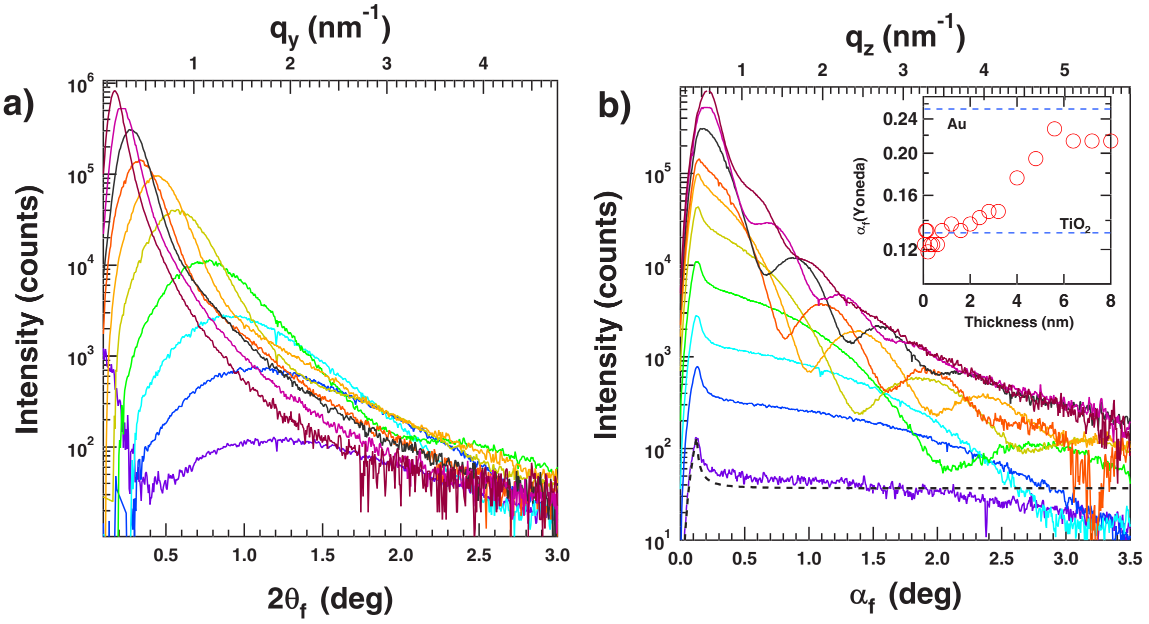

FIG. 7. (Color online) Intensity cross sections of the GISAXS patterns shown in Fig. 6. The cuts are made (a) along the $2\theta_f$ direction at the location of the Yoneda's peak and (b) along α_f at the location of the correlation peak. The intensities have been rescaled accordingly to the counting time. The equivalent thicknesses are (from bottom to top) 0.05, 0.15, 0.3, 0.6, 1.2, 2.0, 2.8, 4.0, 5.6, and 8.0 nm. The inset shows a plot of the Yoneda's peak location as function of deposited thickness, while the dotted curve in (b) corresponds to the transmission function of TiO_2.

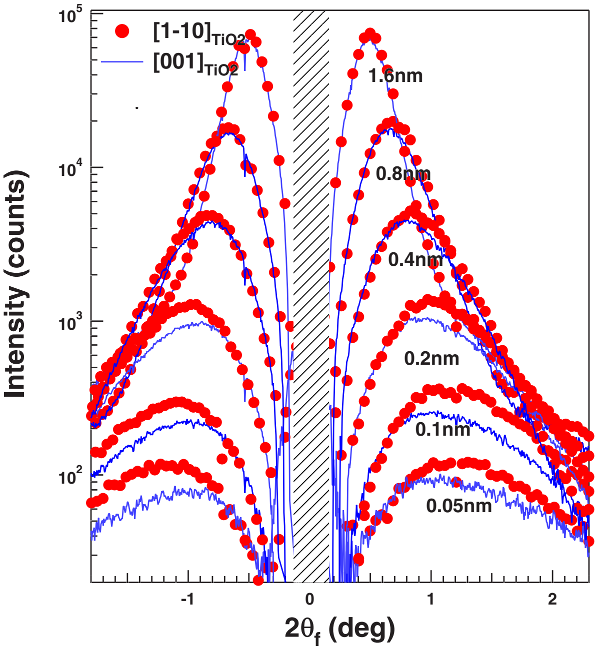

FIG. 8. (Color online) Parallel cross sections of GISAXS patterns acquired with the beam along two crystallographic directions (full circle, $[1\bar{1}0]_{\mathrm{TiO}_2}$; line, $[001]_{\mathrm{TiO}_2}$) at $\alpha_f=3\alpha_c$. A slight anisotropy below the coalescence threshold (0.6 nm) is observed with a higher interparticle distance along $[001]_{\mathrm{TiO}_2}$ than along $[1\bar{1}0]_{\mathrm{TiO}_2}$. The shaded area corresponds to the beam stop limit.

q wave vector transfer range. The "Porod's plot" of the 8 nm film (Fig. 9) demonstrates a power law behavior in the high-q range, $I(q_\parallel)\sim q_\parallel^n$ and $I(q_\perp)\sim q_\perp^m$. If considering only shapes with the z-revolution axis, the found exponents $n=4.02$ and $m=3.63$ are consistent with a truncated sphere profile ($n=4$, $m=2$ for a hemisphere; $n=4$, $m=4$ for a sphere; and $n=3$, $m=2$ for a cylinder[44]). Though it is not such a clear cut at the beginning of the growth, analyses were consistently performed with truncated spheres over the entire study. For the sake of simplicity, the radius R and height H distribution has been taken as a joint-normal law with a correlation coefficient ρ between R and H:

$$\begin{aligned} p(R,H) &= p(R)p(H/R) \\ &= \frac{1}{2\pi\sigma_R\sigma_H\sqrt{1-\rho^2}}\exp\left\{-\frac{(R-\langle R\rangle)^2}{2\sigma_R^2}\right\} \\ &\quad\times\exp\left\{-\frac{\left[H-\left(\langle H\rangle+\rho\frac{\sigma_H}{\sigma_R}(R-\langle R\rangle)\right)\right]^2}{2\sigma_H^2(1-\rho^2)}\right\}. \end{aligned} \tag{4.1}$$

The data have been fitted with the ISGISAXS software[56,64] using a χ^2 criterion, with error bars proportional to the square root of the intensity, as checked from the fluctuations of data points along each cross section.

At each coverage, two cross sections (averaged over a window of five pixels to keep the resolution on the Yoneda's peak) were fitted: (i) along $\alpha_f\sim q_z$ at the correlation peak and

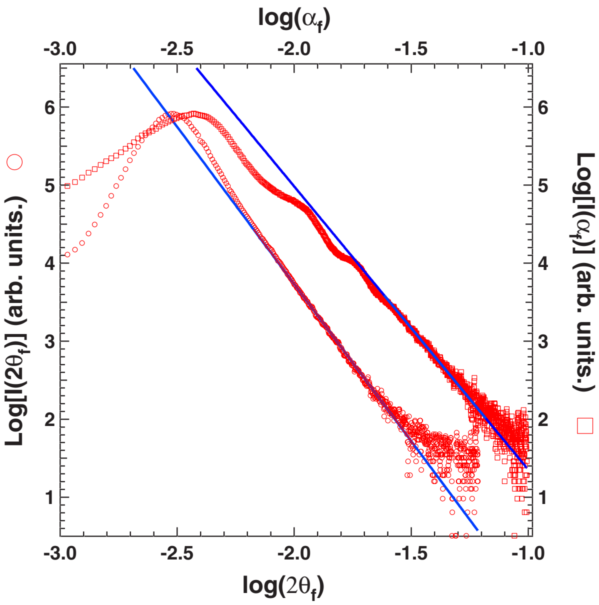

FIG. 9. (Color online) Log-log plot of the cross sections for the 8 nm deposit with a power law fit of the high-q range.

(ii) along $2\theta_f\sim q_y$ at an exit angle α_f equal to three times that of the Yoneda's peak ($\alpha_f=3\alpha_c$). To avoid distortions in fitting the sharp Yoneda's peak, the fit was only performed on data points $\alpha_f>3\alpha_c$. The total χ^2 and the total reliance factor R_B (Ref. 56) always lie below 4 and 0.12, respectively, at any coverage. The SSCA and DWBA models[1] showed an overall good agreement with measured data over four decades of intensity dynamics (Fig. 10). The shape of the correlation peak, the decrease in intensity near the specular rod, and the high-$q_\parallel$ range were well reproduced. The agreement was also good in the perpendicular direction [Fig. 10(b)], except perhaps fringes at the highest coverage. A likely explanation is the oversimplified description of the particle shape and size distribution. If fitted, the incident angle α_i was found close to that determined from sample-beam alignment. The good modeling of the Yoneda's peak (even though not explicitly included in the fitting process) gives confidence in the theoretical treatment of DWBA on the graded interface (see Fig. 17).

The central radius $\langle R\rangle$, central height $\langle H\rangle$, distance between islands D are shown in Fig. 11. The size distribution parameters σ_R, σ_H, and ρ and the SSCA parameters σ_D and κ are given in Figs. 12 and 13. The errors bars stemmed from the curvature of the χ^2 at the minimum. The estimate of the particle spacing $D_p=2\pi/q_y^p$ obtained from the position of the correlation peak q_y^p illustrates the imperious need of a full data analysis since, in a clear effect of interplay between particle form factor and partial interference functions,[1,44,56] D_p is on average 40% higher than the SSCA D value (Fig. 11).

A peculiar attention has been paid to the 1.6 nm film by analyzing the image (Fig. 14) and a series of cross sections (Figs. 15 and 16). A good agreement between experimental and simulated images (Fig. 14) is achieved except near the specular rod. The simulated lobe [Fig. 15(d)] displays a dif-

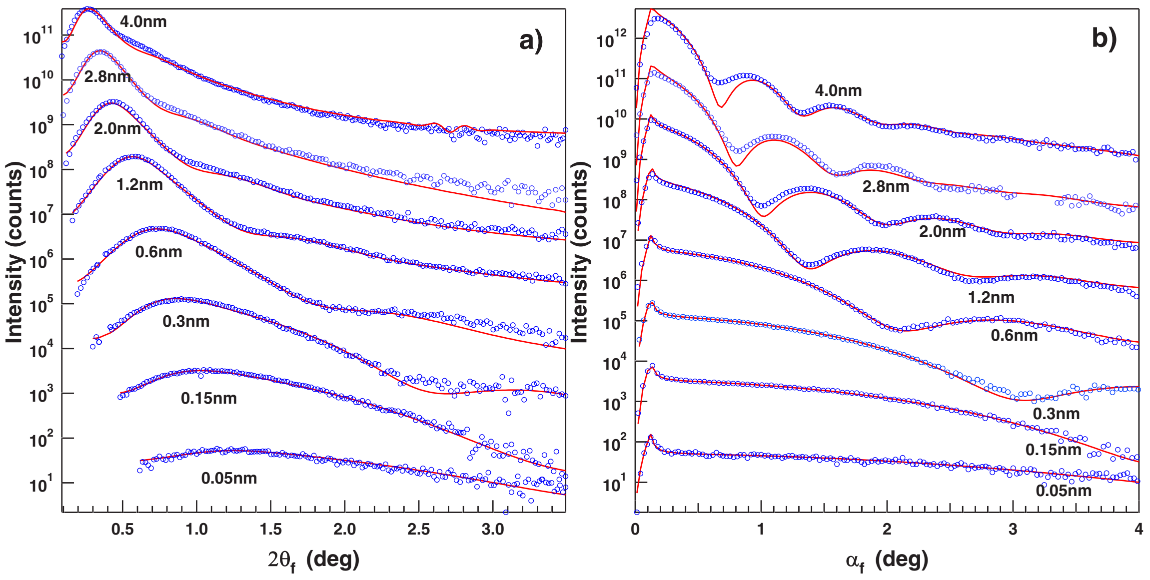

FIG. 10. (Color online) Fits (continuous line) of the GISAXS intensity cross sections (circles) all along the growth. The equivalent deposited thicknesses are given in the figure. Data have been modeled by scattering from size distributed truncated spheres within the SSCA and the DWBA on the graded interface (see text). The curves have been shifted for clarity.

fuse tail due to (i) the interplay between the size-spacing coupling and (ii) the strong correlation between the island radius and height as demonstrated by the plot of their joint-normal probability (see Fig. 16). The discrepancy with the experimental image could result from the beam stop shadowing.

B. Comparison with other approximations

Unsuccessful attempts were made to fit data with the DA, the LMA with a common interference function in each domain (LMA 0), or the DWBA using the flat surface as a reference. Figure 17 exemplifies the discrepancies between the various models for the 1.6 nm thick film. To compare SSCA to DA or LMA 0, the same total spatial disorder $\sigma_D^2(\mathrm{LMA0},\mathrm{DA})=\sigma_D^2(\mathrm{SSCA})+2\kappa^2\sigma_R^2$ was used in the formula [Eq. (2.4)] of the total interference function. As shown in Ref. 1, DA, LMA 0, and SSCA only differ along the correlation peak. Contrary to DWBA on the graded interface,[1] the DWBA applied only to the substrate gives rise to a too sharp Yoneda's peak and to a poorer description of the perpendicular interference fringes.

As correlations seems mandatory to reproduce the scattering line shape, the 1.6 nm curve was fitted with LMA including a correlation between the spacing and the size of the particles in each monodisperse domain.[40] As a matter of comparison, two types of interference functions were used: (i) the 1D paracrystal [Eq. (2.4)] with a linear correlation [Eq. (2.2)] (called LMA 1) and (ii) the 2D interference function of hard disks[65,66] with a hard core radius in each domain that scales with the physical radius $R_{n,\mathrm{HC}}=CR_n$ (called LMA HC). Therefore, for the latter, the actual coverage θ is related to the hard core coverage θ_{HC} used in the interference function through $\theta_{\mathrm{HC}}=C^2\theta$. Even though not analytical,[66] the pair correlation function of interacting 2D hard disks at thermodynamic equilibrium is given satisfactorily by the virial expansion of Ref. 65. The χ^2 and R_B agreement criteria to evaluate the quality of the fit of the data along the $2\theta_f$ direction [Fig. 18(a)] are clearly better with the SSCA ($\chi^2=2.4$,

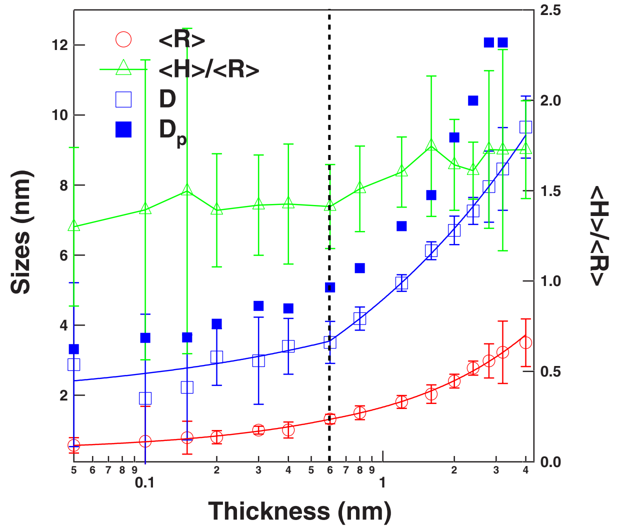

FIG. 11. (Color online) Evolution of the Au/TiO$_2$(110) morphological parameters as function of the deposited thickness: (a) central radius $\langle R\rangle$ (red, open circles), (b) central height over radius $\langle H\rangle/\langle R\rangle$ (green, open triangles), and (c) average spacing between islands D (blue, open square) and the value D_p (blue, filled squares) as deduced from the location of the correlation peak $D_p=2\pi/q_y^p$. The island shape was taken as a truncated sphere and the (R,H) size distribution has been chosen as joint normal. The separation (vertical dotted line) between growth and coalescence is characterized by the power law fits of $\langle R\rangle\sim t^{0.31\pm0.1}$, $t^{0.54\pm0.07}$ and $D\sim t^{0.15\pm0.2}$, $t^{0.51\pm0.05}$ (continuous lines). In passing, note that this corresponds to the onset of decrease of catalytic activity toward the oxidation of CO of Au clusters on TiO$_2$(110) (Ref. 6).

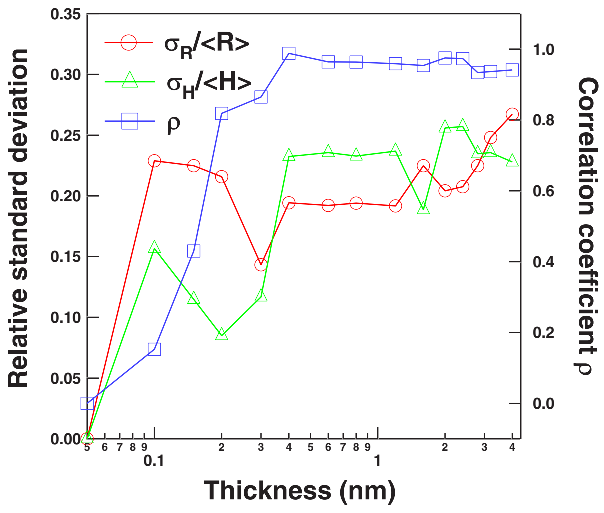

FIG. 12. (Color online) Evolution versus thickness of the joint-normal size distribution parameters Eq. (4.1): $\sigma_R/\langle R\rangle$, $\sigma_H/\langle H\rangle$, and ρ. The mean error bars for $t \geqslant 0.4$ nm are $\frac{\Delta\rho}{\rho}=30\%$, $\frac{\Delta\sigma_R/\langle R\rangle}{\sigma_R/\langle R\rangle}=36\%$, and $\frac{\Delta\sigma_H/\langle H\rangle}{\sigma_H/\langle H\rangle}=140\%$. Below $t<0.4$ nm, the uncertainties are too large. The large error bar on σ_H is explained by the closeness of the correlation coefficient ρ to 1 [see Eq. (4.1)].

$R_B=4.6\%$) than with the LMA 1 ($\chi^2=14.9$, $R_B=11.9\%$) and with the LMA HC ($\chi^2=9.4$, $R_B=8.8\%$). In passing, similar good agreements as well as height parameters are obtained along α_f whatever the approximation. The first conclusion that can be drawn from the parameter values (Table I) is that all approximations agree within the error bars on the most important parameters ($\langle R\rangle, \sigma_R, D$). Note that the mean size $\langle R\rangle$ and size distribution width σ_R are driven by the shape of the scattering curve above the correlation peak. It seems that the data fit is strongly sensitive to the account of correlations (SSCA, LMA 1, and LMA HC). However, the three approximations differ on the spacing parameters and the physical relevance of the morphology used (see Fig. 2). As already shown in Ref. 1, LMA 1 seems to overestimate the role of static disorder σ_D/D, while SSCA and LMA HC find Voronoï's cell nearly proportional to the particle size; indeed, $\sigma_D/D=0.05$ is negligible for SSCA while the packing of particles in LMA HC is very high ($\theta_{\mathrm{HC}}=0.62$) leading to highly ordered monodisperse domains. While the total scattering curve seems to be the same for all the approximations, the discrepancies show up more clearly on the total interference function[40,42] [Fig. 18(b)]. As in previous works,[67–70] a 1D model of scattering (SSCA) from 3D particles was applied to the analysis of scattering from 2D collection of particles. Even if it is difficult to estimate the consequences of such an approximation, the comparison with other hypothesis based on an interference function in 2D shows that the morphology seems accurately obtained within the error bars; the main physics of scattering (i.e., the account of size-spacing correlations in a realistic way) as well as that of the growth mode (see below) seem to be caught. An extension of SSCA to 2D is foreseen in the framework of the 2D ideal paracrystal with disoriented size-limited domains.

V. SELF-SIMILAR ORDERING DURING THE GROWTH OF Au/TiO$_2$(110)

Two regimes can be distinguished in the evolution of $\langle R\rangle$, $\langle H\rangle/\langle R\rangle$, and D upon increasing coverage, with a change in behavior at 0.6–0.8 nm (Fig. 11). Below this value, the spacing between particles $D \sim t^{0.15\pm0.2}$ is nearly constant with respect to the average thickness t. Then, it obeys a power law $D \sim t^{0.51\pm0.05}$. The radius switches from $\langle R\rangle \sim t^{0.31\pm0.1}$ to $\langle R\rangle \sim t^{0.54\pm0.07}$. The particles get more rounded as $\langle H\rangle/\langle R\rangle$ goes from 1.5 to 1.7. The two regimes can be assigned to (i) growth at constant density below 0.6–0.8 nm and (ii) coalescence between compact particles $\langle H\rangle/\langle R\rangle \sim 1.7$ with a

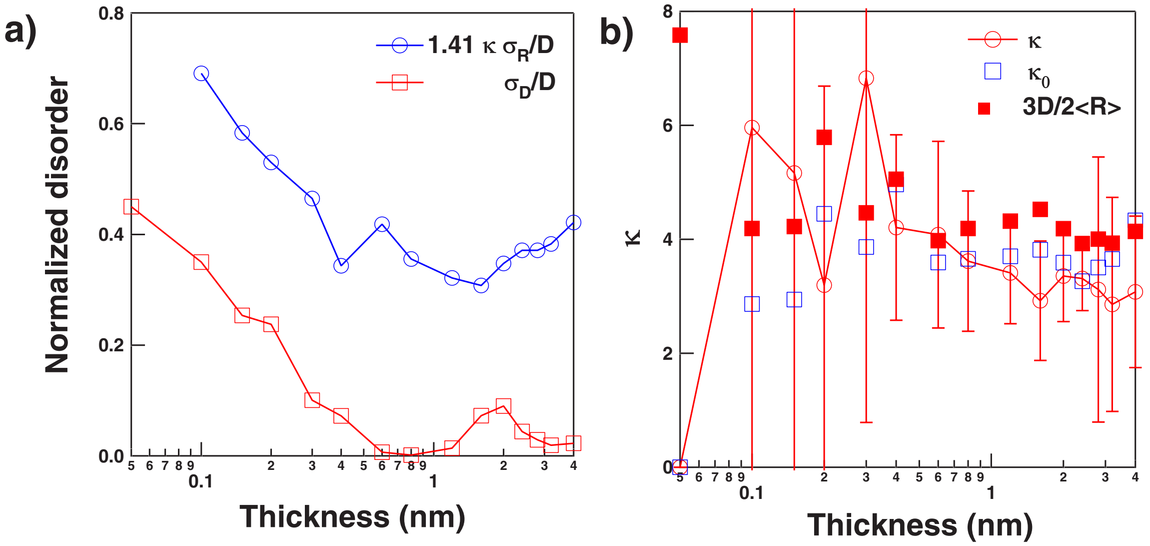

FIG. 13. (Color online) (a) Evolution versus thickness of the two sources of spacing disorder as introduced in the SSCA, namely, the standard deviation of the static paracrystal disorder σ_D/D and of the size-spacing disorder $\sqrt{2}\sigma_R/D$. (b) The size-spacing coupling parameter κ versus the deposited thickness is compared to the special values κ_0 [Eq. 3.20 of Ref. 1] and $3D/2\langle R\rangle$.

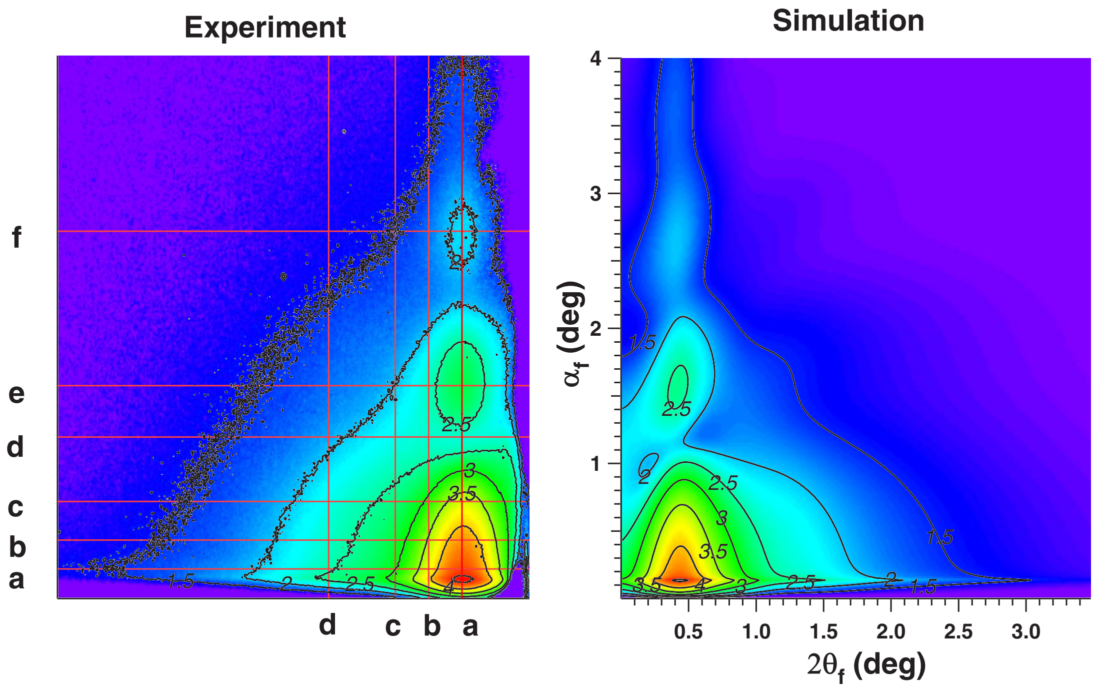

FIG. 14. (Color online) Experimental (left) and simulated (right) GISAXS patterns of 1.6 nm thick deposit. The color scale is logarithmic as given by the contour lines. For a better comparison, the cross sections shown on the experimental image are displayed in Fig. 15 [(a)–(f) along $2\theta_f$ for different α_f] and Fig. 16 [(a)–(d) along α_f for different $2\theta_f$].

nearly constant surface coverage close to 40% but below the jamming limit of 55%–60%.[43,71–73] The nucleation stage could not be characterized because of the smallness of the nuclei[12,17] that gives rises to low and very diffuse scattering.

Complementary studies of the Au/TiO_2(110) system in terms of probed length scales have been performed with *in situ* scanning tunneling microscopy[6,7,10,11,13–15] (STM) and *ex situ* high resolution scanning electron microscopy (HRSEM).[5,17] Below 1 nm, a very good agreement is found between GISAXS and STM (Fig. 6 of Ref. 7) in terms of particle diameter, if assuming a tip convolution of 2 nm. This hypothesis is supported (i) by the comparison of the calibrated thickness with the estimate from STM,[7] (ii) by the difference by a factor of 2 between STM and XPS coverages,[11] and (iii) by the high sensitivity of the STM apparent radius to gap voltage.[10] Moreover, the width of the distribution of radius ($\sigma_R/\langle R\rangle \simeq 0.2$[10,11]) and the maximum of the cluster density (5×10^{12} of Ref. 7) measured by STM agree with the present findings (Fig. 12). STM observations also point to a decrease in the cluster density around 0.4–0.6 nm.[7] However, above 1.5 nm thickness, the present data differ from the HRSEM results that show a wormlike coalescence structure with size and density different by a factor ranging from 5 to 10. The discrepancy could be explained by a different density of defects.

A. Growth laws: Is the coalescence a dynamic process?

The growth process is interrupted during GISAXS acquisitions. Before comparing with theoretical models, it should be determined whether the film might evolve during measurements at 300 K upon coarsening. Notably, no appreciable change in size or shape of Au clusters was seen by STM below $T\sim 800$ K.[7,11] Low-energy ion scattering[19] at $T=775$ K showed a coarsening of gold clusters with a time constant of 25 min. Assuming an activation energy $E_m=3.4$eV/atom (Ref. 21) of the Arnhenius dependence of this time constant, the characteristic time at 300 K appears to be well above the measurement time, which discards coarsening at that temperature, in particular, through Ostwald ripening.

During the first stage at constant particle density, the power law $\langle R\rangle \sim t^{0.31\pm 0.1}$ corresponds to that expected ($\langle R\rangle \sim t^{1/3}$) for particles growing by a diffusion-limited mechanism (and not an attachment limited one) with a negligible direct impingement on the particle and a nearly full condensation.[74,75] A similar result comes from the analytical solution of the growth of a droplet by attachment of diffusing monomers with a constant flux at infinity.[76] The found exponent is closer to that expected from the rate equations of growth[77,78] for a nucleation on defects ($\langle R\rangle \sim t^{1/3}$) than a homogeneous nucleation behavior ($\langle R\rangle \sim t^{2/9}$) in the case of complete condensation. Indeed, on one hand, the sticking coefficient is found close to 1 and, on the other hand, strong re-evaporation would lead to $\langle R\rangle \sim t$ whatever the defect concentration is. The corresponding density of particles $1/D^2 \sim 10^{13}$ cm^{-2} is a typical concentration of defects (vacancies and step edges) on TiO_2(110) surface obtained by ion bombardment and annealing procedure.[4] Nucleation and growth on defects are not a surprise on TiO_2(110) in the light of the literature.[7,8,10,12,16,25–27,79]

The regime observed at higher coverage likely corresponds to coalescence and not to Ostwald ripening (see re-

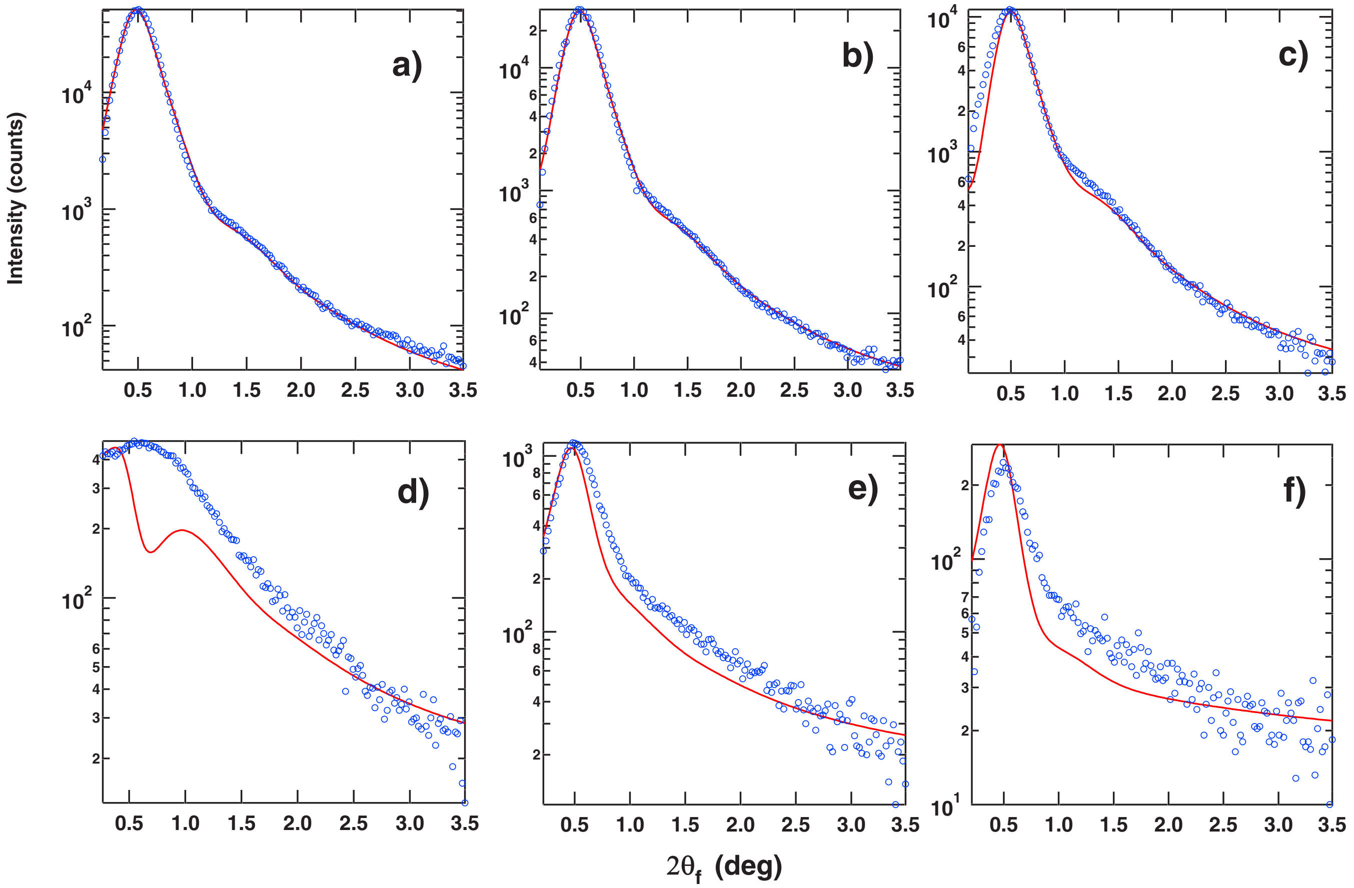

FIG. 15. (Color online) Cross sections along the parallel direction $2\theta_f \sim q_y$ as shown in Fig. 14. Circles are experimental values, and the continuous line corresponds to the simulation.

mark above), i.e., the growth of bigger particles at the expense of the smaller ones through evaporation of atoms driven by the chemical potential difference. Upon arrival of new material on the surface (nonconserved mass system), static and dynamic coalescence mechanisms can occur.[43,80] During static coalescence, neighboring islands merge into a larger particle occupying the center of mass of the two primary particles. If the reshaping time is negligible as compared to the rate of impinging atoms, analytical models, scaling descriptions, and numerical simulations[75,81–83] agree on a $\langle R\rangle \sim t^1$ power law behavior. Power laws relative to the spacing between clusters are more scattered: $D \sim t^1$ (Refs. 72, 75, and 81), $D \sim t^{0.135}$ (Refs. 84 and 85) for homogeneous nucleation, and $D \sim t^{0.5}$ (Ref. 85) for heterogeneous nucleation. Even if the scattering of points in coverage did not allow to check honestly the Vincent's equation of static coalescence which connects the density to the coverage,[81,86,87] the discrepancy with the present exponents rules out the static mechanism. This is supported by a high temperature STM ripening study in which very few clear-cut binary coalescence events were observed.[11]

The dynamic approach of coalescence involves the diffusion of clusters through (i) displacements of edge atoms or evaporation-recondensation mechanisms that move the center of mass of the particle[88–91] for epitaxial clusters or through (ii) a collective motion of the cluster as a whole[92–95] for not well matched particles. Theoretical works of dynamic coalescence of 3D particles on a 2D substrate are scarce.[43] For a mass conserved system, a logarithmic correction was found for the exponents of the power laws $\langle R\rangle$

TABLE I. Morphological parameters corresponding to the fits displayed in Fig. 18 (see text for definitions). θ is the actual coverage, while θ_{HC} is that used in the 2D hard correlation function.

	$\langle R\rangle$ (nm)	$\sigma_R/\langle R\rangle$	D (nm)	σ_D/D	κ	θ	θ_{HC}, C
SSCA	2±0.3	0.23±0.07	6.1±0.4	0.05±0.1	2.9±0.7	0.38±0.4	
LMA 1	2.1±0.3	0.25±0.07	6.0±0.5	0.23±0.05	1.8±0.3	0.38±0.4	
LMA HC	2±0.2	0.31±0.08	6.6±1.6			0.28±0.3	0.62±0.05, 1.5±0.15

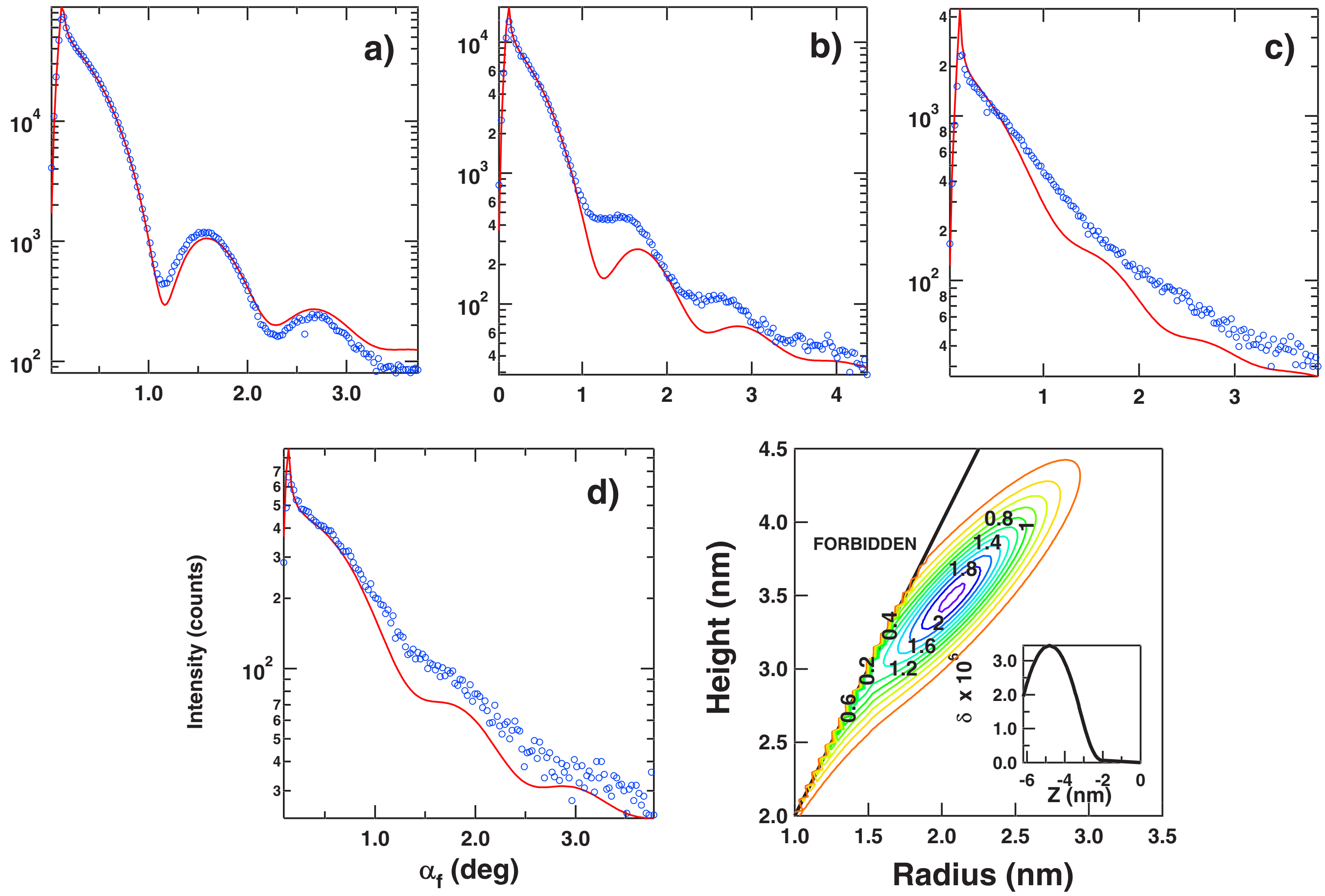

FIG. 16. (Color online) Same as in Fig. 15 but along the perpendicular direction $\alpha_f \sim q_z$. The bottom right figure shows the obtained joint probability of radius and height; the contour levels have been multiplied by 10^3 for clarity. The inset is the perpendicular profile of index of refraction.

$\sim[t/\ln(t)]^{1/3(1-\gamma)}$ and $D \sim [t/\ln(t)]^{1/2(1-\gamma)}$ within simulations in which the Brownian particle diffusion coefficient scales with the volume of the particles, $D_F \sim R^{3\gamma}$ (Ref. 82). Fitting our data leads to $\gamma_R = 0.63 \pm 0.18$ for the radius and $\gamma_D = 0.20 \pm 0.14$ for the distance. The positive values of γ imply an enhanced diffusion of the biggest clusters. This runs counter the usual expectations for 2D epitaxial islands,[89–91,96] in particular, for the metal-metal systems.[97] However, surprisingly high mobilities of particles containing thousands of atoms have already been observed (i) experimentally for clusters preformed in gas phase and deposited on substrate[98,99] or for Au evaporated on amorphous alumina[83] and (ii) theoretically with some molecular dynamics simulations of not well matched 3D particles[92–95,100] for which slip diffusion and Levy's flights have been predicted. Indeed, as in those cases, the $Au/TiO_2(110)$ interface was found to be poorly matched with a low adhesion energy (see Sec. III and Sec. V C). Moreover, it is argued that complexes formed by vacancies and gold clusters are the diffusing entities on $TiO_2(110)$ above a critical size.[12] The dynamic model of Steyer *et al.*[76] introduces a random motion of clusters with a size-dependent diffusion coefficient in a nonconserved mass framework. At low surface coverage, a bimodal size distribution was found, in which the small particles grow by a diffusion-limited mechanism $\langle R_{small} \rangle \sim t^{0.33}$ while the large particles follow $\langle R \rangle \sim t^{0.48}$ and $D \sim t^{0.25}$, in close agreement with the present measurement for the radius ($\langle R \rangle \sim t^{0.54}$) but not for the interparticle distance ($D \sim t^{0.51}$). Although the present data escape the static coalescence model, the existing dynamical approaches fail to fully account for them, maybe because depinning from traps and diffusion of clusters is only efficient above a critical size.[83,101]

B. Self-similar behavior and spatial ordering during coalescence

The self-similar behavior of the coalescence is clearly illustrated by rescaling the scattering curves (Fig. 19) with the intensity and position of the correlation peak.[102] Above $t \sim 0.6$ nm, the scaled scattering follows a master curve along the parallel and the perpendicular directions. In other words, the overall morphology of the particle collection is the same at different evaporation times within a length scale factor. This conclusion is supported by the full data analysis once the quantities are rescaled by the mean values: cluster size distribution widths (Fig. 12) and components of spatial disorder (Fig. 13).

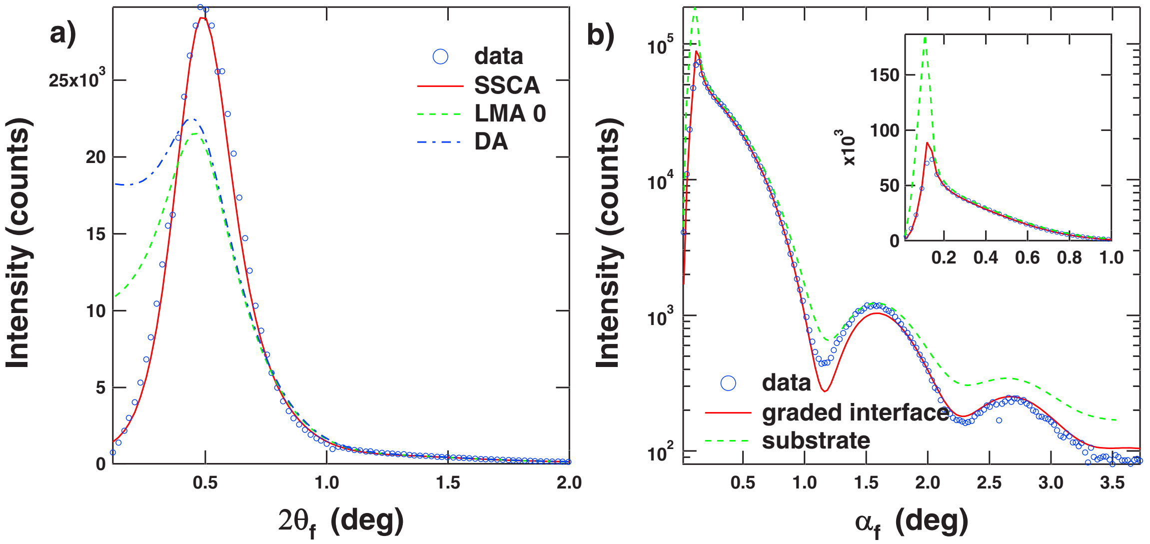

FIG. 17. (Color online) Comparison between the various models for the 1.6 nm thick deposit with the same morphological parameters. Experimental points and computed scattering curves along (a) the parallel direction using SSCA, DA, and LMA 0 with a common interference function [Eq. (2.4)] in each domain (linear scale) (b) the perpendicular direction using DWBA on the graded interface and on the flat substrate only (the same curves are displayed in the inset on a linear scale). The interference function of the paracrystal [Eq. (2.4), Ref. 37] with a similar total disorder as in the SSCA [$\sigma_D^2(\mathrm{LMA0,DA})=\sigma_D^2(\mathrm{SSCA})+2\kappa^2\sigma_R^2$] was used for the DA and LMA simulations.

The transition from growth to coalescence is also seen by plotting the two components of the variance of the particle spacing: $\langle(d_n-D)^2\rangle/D^2=\sigma_D^2/D^2+2\kappa^2\sigma_R^2/D^2$ [Fig. 13(a)]. The first term, σ_D/D, is linked to the intrinsic spacing disorder of the SSCA paracrystal. In terms of growth, this is the randomness of the spatial distribution of the particles due to heterogeneous nucleation centers. The second term, $\sqrt{2}\kappa\sigma_R/D$, is the component of the spatial disorder which arises from the correlations between the size and the influence area (depleted zone) of the particles.

During growth and coalescence, the dynamic disorder $\sqrt{2}\kappa\sigma_R/D$ dominates over the static disorder σ_D/D that falls down below a negligible value for increasing coverage (Fig. 13). A consistent explanation is that the growth-coalescence mechanism does not keep too much in memory the initial spatial disorder of nucleation centers and, furthermore, induces a spatial ordering of the particles as $\sqrt{2}\kappa\sigma_R/D$ decreases from ~70% down to 40%. Since, during the coalescence stage, the distance between clusters is proportional to their radius ($D\sim\langle R\rangle^{0.9\pm0.1}$), $\kappa\sim3.3$ and $\sigma_D/D\sim0$ are nearly constant [Fig. 13(b)], the Voronoï cell of each particle scales with its radius.[103] This provides an additional argument to discard the static mechanism, since the static coalescence of growing particles would keep the static spatial disorder due to the randomness of nucleation centers. This instead favors a dynamic process involving diffusing species captured by particles with a cross section proportional to Voronoï cell diameter. Such proportionality is a key ingredient in the standard model of rate equations of growth[77] to go beyond the mean field results; indeed, using capture numbers that depend on the island sizes allows to implicitly include the lacking physics, i.e., the island correlation.[48–54] Comparing kinetic Monte Carlo simulations of coalescence of 2D islands with models of mean field kinetic theory of growth, Liu *et al.*[104] concluded that the correlation between the locations of islands strongly affects the coalescence rate as compared to randomly located particles.

The normalized location disorder $\sqrt{2}\kappa\sigma_R/D$ (Fig. 13) as well as the relative radius and height distributions $\sigma_R/\langle R\rangle\sim\sigma_H/\langle H\rangle$ (Fig. 12) are nearly constant during the coalescence. This indicates that both the cluster size distribution and the cluster spatial distribution behave in a self-similar way. Scaling arguments over the size distribution are often encountered in processes of static coalescence,[80] dynamic coalescence in non-mass-conserved system, and also for pure Ostwald ripening or for coarsening during phase separation.[43,102] Through Monte Carlo simulations of growth and static coalescence, Mulheran and Blackman[48] argued that the proportionality between the island Voronoï cell size and the particle radius is at the heart of the observed scaling behavior. However, to our knowledge, this self-similar behavior on the position of particles was scarcely highlighted. Carlow and Zinke-Allmang[105–107] experimentally showed that Sn/Si(111) clusters at low coverage (10%) evolve upon Ostwald ripening toward a spatial and size ordered state where the islands are self-organized into a scale invariant configuration. This was thereafter theoretically explained by Tarr and Mulheran[108] as the result of the reabsorption (or pedophagous) effect where island releasing monomers reabsorb their own offspring. In their simulation, the spatial ordering appears as a ubiquitous phenomenon of ripening that is not sensitive to atomistic detail of monomer release or to the starting configuration. However, for Au clusters on $TiO_2(110)$, such a spatial ordering phenomenon is herein observed upon coalescence in non-mass-conserved system instead of during ripening.

An other clue about self-similar behavior appears in the evolution of the correlation parameter κ [Fig. 13(b)]. During

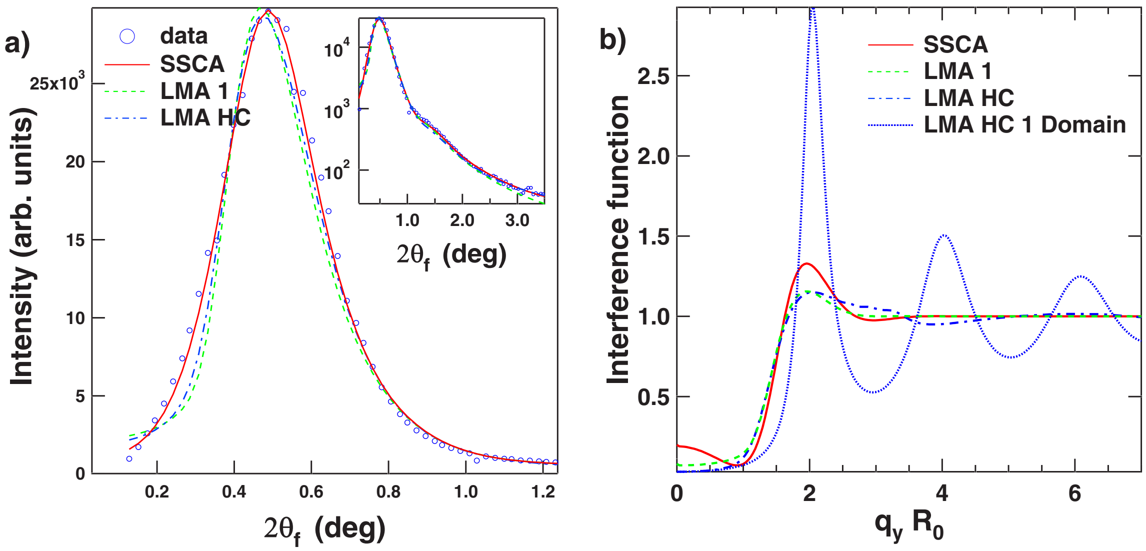

FIG. 18. (Color online) (a) Comparison of the fits of the parallel scattering curve $\alpha_f = \alpha_c$ of 1.6 nm thick deposit using various models of correlations: (i) SSCA, (ii) LMA 1 using a paracrystal interference function [Eq. (2.4)] that includes a linear correlation between the mean distance and the size in each monodisperse domain [Eq. (2.2)], and (iii) LMA HC using a 2D hard core interference function with a hard core radius in each domain that scales with the physical radius $R_{n,\mathrm{HC}} = CR_n$. The other hypotheses of the fit are those of Sec. IV. The same curves are displayed in the inset on a logarithmic scale and the morphological parameters are given in Table. I. (b) Corresponding total interference functions $S(q_y\langle R\rangle)$.

the growth, the scale factor κ is close to $\kappa_0(\mathbf{q}_\perp = 0) \simeq 3D/2\langle R\rangle$ that leads to the minimum of scattered intensity at the vicinity of the specular rod.[1] As explained in the Appendix, this characterizes a mechanism of growth and coalescence with a share out of matter proportional to the size of each particle. The rule seems to be better fulfilled during the coalescence than during the growth stage during which the capture areas of the islands still feel the randomness of the nucleation centers.

C. Equilibrium shape and adhesion energy

During the coalescence stage, the aspect ratio $\langle H\rangle/\langle R\rangle$ is nearly constant while the correlation coefficient ρ between the particle height and radius is close to 1; this indicates that clusters are close to equilibrium (Fig. 12). The fast reshaping of the clusters with respect to the growth rate and release of monomers excludes the appearance of wormlike structures. In addition, gold films deposited at 300 K and then annealed 2 min at 850 K (Fig. 20) hardly show any aspect ratio

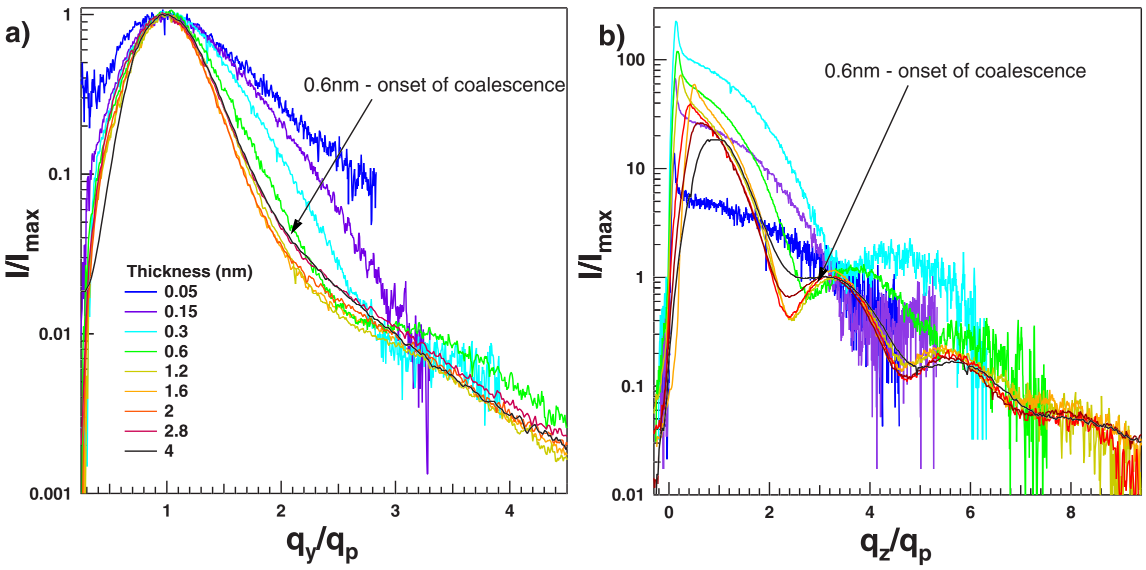

FIG. 19. (Color online) Self-similarity evidence obtained upon scaling the (a) parallel and (b) perpendicular scattering cross sections (Fig. 7) with the q_y^p location of the correlation peak. Above 0.6 nm, i.e., during coalescence, the scaled scattering follows a master curve. Note that the curves along the q_z direction have been rescaled by the intensity of the first scattering lobe to avoid multiple scattering effect of the Yoneda's peak.

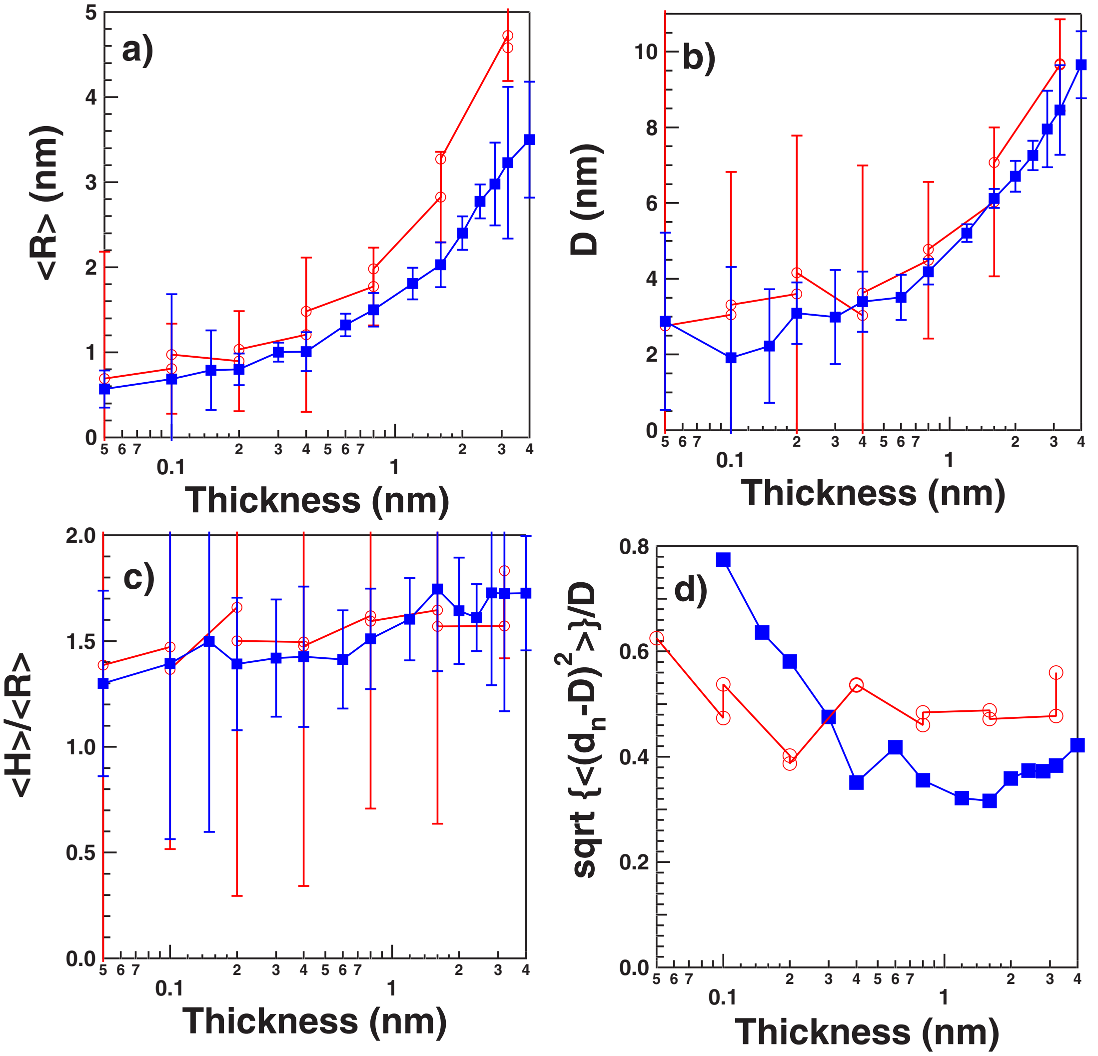

FIG. 20. (Color online) Comparison of the Au/TiO$_2$(110) morphological parameters obtained during standard growth at room temperature (filled square) and for the flash annealing procedure (open circle). (a) Mean particle radius $\langle R\rangle$. (b) Spacing between islands D. (c) Particle aspect ratio $\langle H\rangle/\langle R\rangle$. (d) Standard deviation of the fluctuations of particle spacing, $\sqrt{\langle(d_n-D)^2\rangle}/D=\sqrt{\sigma_D^2+2\kappa^2\sigma_R^2}/D$ (see text and Ref. 1).

$\langle H\rangle/\langle R\rangle$ variation with respect to room temperature deposition. The annealing induces only a ripening of the nanoparticles with an increase of ~20% of the island size, a decrease of ~25% of the island density, and a different behavior of the spatial location disorder.

The truncated sphere shape and the full size distribution allow us to calculate a mean contact angle θ_c and an adhesion energy from the Young-Dupré formula $E_{adh}=\gamma_{\mathrm{Au}}(1+\cos\theta_c)$, where $\gamma_{\mathrm{Au}}=1.131\ \mathrm{J/m^{-2}}$ is the surface energy of gold,[60] as a function of the coverage (Fig. 21). The value of $\theta_c=130°\pm5°$ for the contact angle of large particles is in good agreement with the value of $\theta_c=122°\pm5°$ obtained by (i) Zhang *et al.*[5,17] combining high resolution scanning electron microscopy, quartz microbalance measurements, and transmission electron microscopy and (ii) Chatain *et al.*[109] by the sessile drop method with molten gold. The discrepancy with *ab initio* calculation,[24] which suggests an adhesion energy close to zero, could come from the pinning of the clusters on vacancies or step edges.[12,25–27]

The present finding of a change in contact angle (adhesion) around a mean size of $\langle R\rangle\sim1.3$ nm (~500 atoms/cluster, average thickness of 0.6 nm in Fig. 11) at the onset of the particle coalescence is compatible with the transition from "flat" 3D shape to spherical 3D shape around a coverage of 0.4–0.6 nm.[5,7] The GISAXS measurements are less sensitive to the 2D or quasi-two-dimensional particles seen by low-energy ion scattering[19] or scanning tunneling microscopy.[7] These quasi-two-dimensional particles are dispersed on terraces and appear at the early beginning of the growth (below 0.2 nm); their height is between 1 and 3 ML. However, they are, in fact, mixed with flat 3D clusters that mainly grow along the step edges,[7,12] a fact that may explain the slight GISAXS anisotropy observed at the beginning of the growth on the mean spacing between particles in the $[1\bar{1}0]_{\mathrm{TiO}_2}$ and $[001]_{\mathrm{TiO}_2}$ directions (Fig. 8). The morphological transition from 2D or quasi-two-dimensional to flat 3D particles was interpreted by a stabilization of flat 3D par-

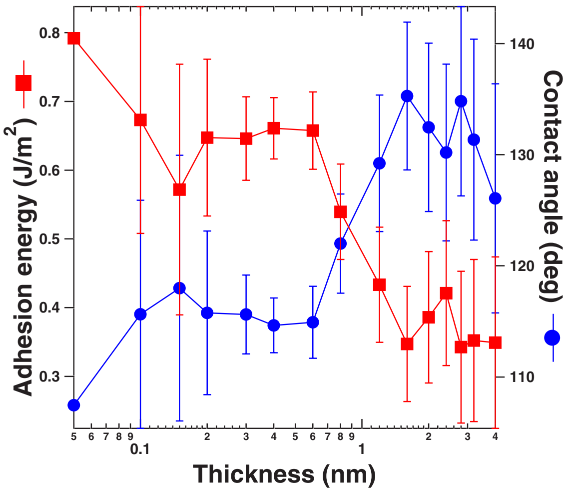

FIG. 21. (Color online) Evolution of the adhesion energy E_{adh} (left scale) as deduced from the contact angle θ_c (right scale) using the Young-Dupré formula. The error bars are given by the variance of the value over the obtained size distribution.

ticles, thanks to an accumulation of vacancies on the substrate below the particles.[12]

It is also of interest to note that the size-sensitive catalytic oxidation of CO by gold particles supported on titania passes through a maximum of activity for a cluster radius of 1.5 nm,[6] which corresponds to the end of the growth and onset of the coalescence. Indeed, the growing clusters which were until that point pinned on defects, as indicated by their density, begin to coalesce via a dynamic mechanism dominated by diffusion processes.

VI. CONCLUSIONS

The crystallographic structure and morphology of gold nanoparticles on $TiO_2(110)$ surface have been explored *in situ* during the growth by using grazing incidence x-ray scattering techniques. Complex epitaxial orientations have been observed with a pinning of the dense direction $[1\bar{1}0]_{\mathrm{Au}}$ of gold along the bridging oxygen row direction $[001]_{\mathrm{TiO}_2}$. Models including (i) the scaling of the particle spacing on their size (size spacing correlation approximation) and (ii) multiple scattering along the graded interface were applied to the analysis of the diffuse scattering from a dense collection of gold nanoparticles; they were shown to catch the essential features of the growth mode, namely, the growth at constant density limited by surface diffusion followed by a coalescence mechanism at constant equilibrium shape with a self-similar behavior of not only the size distribution but also the spatial ordering. The above findings suggest that the change in the catalytic behavior of $Au/TiO_2(110)$ at a cluster radius of 1.5 nm is associated with the onset of the coalescence of gold particles. Consistently, the coalescence involves a change in shape from flat 3D to 3D of the particles and the switch from particles pinned by surface defects to self-similar growing particles. These findings on the growth and coalescence mechanisms are in agreement and complementary to near-field microscopy that focuses on the early stages of the growth. They demonstrate the sensitivity of the GISAXS technique to particle layer morphology. The outlook in terms of future experiments is the monitoring of gas induced sintering of supported nanoparticles during a catalytic reaction, that is to say bridging the pressure gap and reaching more realistic conditions of aging studies of catalysts.

ACKNOWLEDGMENTS

The technical assistance of the BM32 beamline team was invaluable during synchrotron experiments. This work was partly funded by the French Ministry of Research (program "ACI-nanotechnologie," project NanoCat).

APPENDIX: SIMPLE MODEL FOR THE SIZE-SPACING COUPLING IN ONE DIMENSION

This appendix aims at demonstrating that the formulation of the 1D size-spacing coupling[1] and the special value of the coupling parameter κ_0 can be recovered using simple hypothesis of material conservation.

Let us consider a 1D chain of particles indexed by n. The central hypothesis is that all the material inside neighboring particles is proportional to the length d_n of the "unit cell." In terms of growth, all the atoms falling inside the unit cell are captured by the neighboring particles. With the assumption that the volume of each particle is proportional to its in-plane radius R_n, $V_n = \nu R_n^3$ (ν is constant[110]), one ends up with

$$d_n = \frac{1}{2}\frac{\nu}{\Omega}[R_{n-1}^3 + R_n^3], \qquad \text{(A1)}$$

where Ω is the quantity of matter per unit of length. The coefficient $1/2$ implies an equal distribution of matter between the nth and $(n-1)$th particles. This supposes that the fluctuations of particle radius and of the distances between neighboring particles are so small that the situation is not so far from the regular lattice of monodispersed particles. A first order expansion in the fluctuations of sizes around the mean value $\langle R_n \rangle$ gives

$$d_n = \frac{\nu}{\Omega}\langle R_n \rangle^3 \left[1 + \frac{3}{2\langle R_n \rangle}(\Delta R_{n-1} + \Delta R_n)\right]. \qquad \text{(A2)}$$

Noticing that $\langle d_n \rangle = \frac{\nu}{\Omega}\langle R_n \rangle^3$, Eq. (3.10) of Ref. 1 with $\kappa_0 = 3\langle d_n \rangle / 2\langle R_n \rangle$ is recovered. This value corresponds exactly to the expansion for low size distribution of the special value κ_0 that leads to a minimum of scattering at $q_\parallel = 0$.

[*] Corresponding author. remi.lazzari@insp.jussieu.fr

[†] grenaud@cea.fr

[‡] jacques.jupille@insp.jussieu.fr

[§] leroy@crmcn.univ-mrs.fr

[1] R. Lazzari, F. Leroy, and G. Renaud, Phys. Rev. B **76**, 125411 (2007).

[2] M. Haruta and M. Date, Appl. Catal., A **222**, 427 (2001).

[3] T. Choudhary and D. Goodman, Appl. Catal., A **291**, 32 (2005).

[4] U. Diebold, Surf. Sci. Rep. **48**, 53 (2003).

[5] F. Cosandey and T. Madey, Surf. Rev. Lett. **8**, 73 (2001).

[6] M. Valden, X. Lai, and D. W. Goodman, Science **281**, 1647 (1998).

[7] X. Lai, T. St Clair, M. Valden, and D. Goodman, Prog. Surf. Sci. **59**, 25 (1998).

[8] X. Lai and D. Goodman, J. Mol. Catal. A: Chem. **162**, 33 (2000).

[9] A. Kolmakov and D. W. Goodman, Surf. Sci. **490**, L597 (2001).

[10] N. Spiridis, J. Haber, and J. Korecki, Vacuum **63**, 99 (2001).

[11] C. Mitchell, A. Howard, M. Carney, and R. Edgell, Surf. Sci. **490**, 196 (2001).

[12] E. Wahlström, N. Lopez, R. Schaub, P. Thostrup, A. Rønnau, C. Africh, E. Lægsgaard, J. K. Nørskov, and F. Besenbacher, Phys. Rev. Lett. **90**, 026101 (2003).

[13] A. Santra, F. Yang, and D. Goodman, Surf. Sci. **548**, 324 (2004).

[14] Y. Maeda, T. Fujitani, S. Tsubota, and M. Haruta, Surf. Sci. **562**, 1 (2004).

[15] T. Minato, T. Susaki, S. Shiraki, H. Kato, K. Kawai, and M. Aika, Surf. Sci. **566-568**, 1012 (2004).

[16] W. Wallace, B. Min, and D. Goodman, J. Mol. Catal. A: Chem. **228**, 3 (2005).

[17] L. Zhang, F. Cosandey, R. Persaud, and T. Madey, Surf. Sci. **439**, 73 (1999).

[18] F. Cosandey, L. Zhang, and T. Madey, Surf. Sci. **474**, 1 (2001).

[19] L. Zhang, R. Persaud, and T. Madey (unpublished).

[20] Y. Yoshihara, S. C. Parker, and C. T. Campbell, Surf. Sci. **439**, 153 (1999).

[21] C. T. Campbell, S. C. Parker, and D. E. Starr, Science **298**, 811 (2002).

[22] Z. Yang, R. Wu, and D. W. Goodman, Phys. Rev. B **61**, 14066 (2000).

[23] L. Giordano, G. Pacchioni, T. Bredow, and J. Fernández Sanz, Surf. Sci. **471**, 21 (2001).

[24] N. Lopez and J. Nørskov, Surf. Sci. **515**, 175 (2002).

[25] Y. Wang and G. Hwang, Surf. Sci. **542**, 72 (2003).

[26] N. Lopez, J. K. Nørskov, T. V. W. Janssens, A. Carlsson, A. Puig-Molina, B. Clausen, and J.-D. Grunwaldt, J. Catal. **225**, 86 (2004).

[27] D. Pillay and G. S. Hwang, Phys. Rev. B **72**, 205422 (2005).

[28] V. Holý, U. Pietsch, and T. Baumbach, *High-resolution X-Ray Scattering from Thin Films and Multilayers*, Springer Tracts in Modern Physics Vol. 149 (Springer, New York, 1998).

[29] J. Daillant and A. Gibaud, *X-Ray and Neutron Reflectivity: Principle and Applications*, Lectures Notes in Physics (Springer, New York, 1999).

[30] S. K. Sinha, E. B. Sirota, S. Garoff, and H. B. Stanley, Phys. Rev. B **38**, 2297 (1988).

[31] M. Rauscher, T. Salditt, and H. Spohn, Phys. Rev. B **52**, 16855 (1995).

[32] M. Rauscher, R. Paniago, H. Metzger, Z. Kovats, H. D. Domke, J. Pfannes, J. Schulze, and I. Eisele, J. Appl. Phys. **86**, 6763 (1999).

[33] J. S. Pedersen, P. Vysckocil, B. Schönfeld, and G. Kostorz, J. Appl. Crystallogr. **30**, 975 (1997).

[34] A. Guinier and G. Fournet, *Small-Angle Scattering of X-Rays* (Wiley, New York, 1955).

[35] G. Glatter and O. Kratky, *Small Angle X-Ray Scattering* (Academic, New York, 1982).

[36] A. Guinier, *X-Ray Diffraction in Crystals, Imperfect Crystals and Amorphous Bodies* (Dover, New York, 1963).

[37] R. Hosemann and S. N. Bagchi, *Direct Analysis of Diffraction by Matter* (North-Holland, Amsterdam, 1962).

[38] M. Kotlarchyk and S.-H. Chen, J. Chem. Phys. **79**, 2461 (1983).

[39] C. Vonk, J. Appl. Crystallogr. **9**, 433 (1976).

[40] J. S. Pedersen, J. Appl. Crystallogr. **27**, 595 (1994).

[41] W. Bertram, J. Appl. Crystallogr. **29**, 682 (1996).

[42] D. Gazzillo, A. Giacometti, R. Guido Della Valle, F. Venutti, and E. Carsughi, J. Chem. Phys. **111**, 7636 (1999).

[43] M. Zinke-Allmang, Thin Solid Films **346**, 1 (1999).

[44] C. Revenant, F. Leroy, R. Lazzari, G. Renaud, and C. R. Henry, Phys. Rev. B **69**, 035411 (2004).

[45] R. Hosemann, Acta Crystallogr. **4**, 520 (1951).

[46] R. Hosemann and A. Hindeleh, J. Macromol. Sci., Phys. **B34**, 327 (1995).

[47] R. Millane and J. Eads, Acta Crystallogr., Sect. A: Found. Crystallogr. **A56**, 497 (2000).

[48] P. A. Mulheran and J. A. Blackman, Phys. Rev. B **53**, 10261 (1996).

[49] M. C. Bartelt and J. W. Evans, Phys. Rev. B **54**, R17359 (1996).

[50] J. G. Amar, M. N. Popescu, and F. Family, Phys. Rev. Lett. **86**, 3092 (2001).

[51] P. A. Mulheran and D. A. Robbie, Phys. Rev. B **64**, 115402 (2001).

[52] F. G. Gibou, C. Ratsch, M. F. Gyure, S. Chen, and R. E. Caflisch, Phys. Rev. B **63**, 115401 (2001).

[53] J. W. Evans and M. C. Bartelt, Phys. Rev. B **66**, 235410 (2002).

[54] F. Gibou, C. Ratsch, and R. Caflisch, Phys. Rev. B **67**, 155403 (2003).

[55] R. Baudoing-Savois, M. De Santis, M. Saint-Lager, O. Dolle, P. Geaymond, P. Taunier, P. Jeantet, J. Roux, G. Renaud, and A. Barbier, Nucl. Instrum. Methods Phys. Res. B **149**, 213 (1999).

[56] R. Lazzari, J. Appl. Crystallogr. **35**, 406 (2002).

[57] T. Akita, M. Okumura, K. Tanaka, and M. Haruta, J. Catal. **212**, 119 (2002).

[58] C. Wang, Y. Zhang, V. Shutthanandan, S. Thevuthasan, and G. Duscher, J. Appl. Phys. **95**, 8185 (2004).

[59] J. Olander, R. Lazzari, J. Jupille, B. Mangili, J. Goniakowski, and G. Renaud, Phys. Rev. B **76**, 075409 (2007).

[60] C. T. Campbell, Surf. Sci. Rep. **27**, 1 (1997).

[61] G. Renaud, M. Ducruet, O. Ulrich, and R. Lazzari, Nucl. Instrum. Methods Phys. Res. B **222**, 667 (2004).

[62] Y. Yoneda, Phys. Rev. **131**, 2010 (1963).

[63] I. Kegel, T. H. Metzger, A. Lorke, J. Peisl, J. Stangl, G. Bauer, K. Nordlund, W. V. Schoenfeld, and P. M. Petroff, Phys. Rev. B **63**, 035318 (2001).

[64] R. Lazzari, ISGISAXS, 2002, http://www.esrf.fr/computing/scientific/joint_projects/IsGISAXS

[65] M. Baus and J. L. Colot, Phys. Rev. A **36**, 3912 (1987).

[66] S. C. Wu, D. T. Wasan, and A. D. Nikolov, Phys. Rev. E **71**, 056112 (2005).

[67] I. Kegel, T. H. Metzger, and J. Peisl, Appl. Phys. Lett. **74**, 2978 (1999).

[68] M. Mâaza, A. Gibaud, C. Sella, B. Pardo, J. A. B. F. Dunsteter, F. Corno, G. Vignaud, A. Désert, and A. Menelle, Eur. Phys. J. B **7**, 339 (1999).
[69] A. Gibaud, S. Hazra, C. Sella, P. Laffez, A. Désert, A. Naudon, and G. Van Tendeloo, Phys. Rev. B **63**, 193407 (2001).
[70] S. Narayanan, D. R. Lee, R. S. Guico, S. K. Sinha, and J. Wang, Phys. Rev. Lett. **94**, 145504 (2005).
[71] M. Bartelt and J. Evans, Surf. Sci. **298**, 421 (1993).
[72] J. Carrey and J. L. Maurice, Phys. Rev. B **63**, 245408 (2001).
[73] J. Carrey and J. L. Maurice, Phys. Rev. B **65**, 205401 (2002).
[74] B. Chakraverty, J. Phys. Chem. Solids **28**, 2413 (1967).
[75] J. L. Viovy, D. Beysens, and C. M. Knobler, Phys. Rev. A **37**, 4965 (1988).
[76] A. Steyer, P. Guenoun, D. Beysens, and C. M. Knobler, Phys. Rev. A **44**, 8271 (1991).
[77] J. A. Venables, Philos. Mag. **27**, 697 (1973).
[78] P. Jensen, H. Larralde, M. Meunier, and A. Pimpinelli, Surf. Sci. **412-413**, 458 (1998).
[79] B. Min, W. Wallace, and D. Goodman, Surf. Sci. **600**, L7 (2006).
[80] M. Zinke-Allmang, L. Feldman, and M. Grabow, Surf. Sci. Rep. **16**, 377 (1992).
[81] B. J. Briscoe and K. P. Galvin, Phys. Rev. A **43**, 1906 (1991).
[82] P. Meakin, Rep. Prog. Phys. **55**, 157 (1992).
[83] J. Carrey, J. L. Maurice, F. Petroff, and A. Vaurès, Phys. Rev. Lett. **86**, 4600 (2001).
[84] F. Family and P. Meakin, Phys. Rev. Lett. **61**, 428 (1988).
[85] F. Family and P. Meakin, Phys. Rev. A **40**, 3836 (1989).
[86] R. Vincent, Proc. R. Soc. London, Ser. A **321**, 53 (1971).
[87] M. Fanfoni, M. Tomellini, and M. Volpe, Phys. Rev. B **64**, 075409 (2001).
[88] J. C. Hamilton, Phys. Rev. Lett. **77**, 885 (1996).
[89] A. Bogicevic, S. Liu, J. Jacobsen, B. Lundqvist, and H. Metiu, Phys. Rev. B **57**, R9459 (1998).
[90] T. Mattsson, G. Mills, and H. Metiu, J. Chem. Phys. **110**, 12151 (1999).
[91] G. Mills, T. Mattsson, L. Møllnitz, and H. Metiu, J. Chem. Phys. **111**, 8639 (1999).
[92] P. Deltour, J. L. Barrat, and P. Jensen, Phys. Rev. Lett. **78**, 4597 (1997).
[93] W. D. Luedtke and U. Landman, Phys. Rev. Lett. **82**, 3835 (1999).
[94] L. J. Lewis, P. Jensen, N. Combe, and J. L. Barrat, Phys. Rev. B **61**, 16084 (2000).
[95] P. Jensen, A. Clément, and L. J. Lewis, Physica E (Amsterdam) **21**, 71 (2004).
[96] S. V. Khare and T. L. Einstein, Phys. Rev. B **54**, 11752 (1996).
[97] H. Brune, Surf. Sci. Rep. **31**, 121 (1998).
[98] L. Bardotti, P. Jensen, A. Hoareau, M. Treilleux, and B. Cabaud, Phys. Rev. Lett. **74**, 4694 (1995).
[99] I. Goldby, L. Kuipers, B. von Issendorff, and R. Palmer, Appl. Phys. Lett. **69**, 2819 (1996).
[100] P. Jensen, Rev. Mod. Phys. **71**, 1695 (1999).
[101] A. Gates and J. Robins, Thin Solid Films **149**, 113 (1987).
[102] P. Fratzl, J. L. Lebowitz, O. Penrose, and J. Amar, Phys. Rev. B **44**, 4794 (1991).
[103] J. C. Zanghi, J. J. Métois, and R. Kern, Surf. Sci. **52**, 556 (1975).
[104] S. Liu, L. Bönig, and H. Metiu, Surf. Sci. **392**, L56 (1997).
[105] G. R. Carlow and M. Zinke-Allmang, Phys. Rev. Lett. **78**, 4601 (1997).
[106] G. Carlow, Physica A **239**, 65 (1997).
[107] K. Shorlin, M. Zinke-Allmang, and D. Fraser, Phys. Rev. B **66**, 165403 (2002).
[108] D. Tarr and P. Mulheran, Phys. Rev. E **68**, 020602 (2003).
[109] F. Chabert, J. Fouletier, and D. Chatain, *Wettability of different titanium oxides by gold under an oxygen-controlled gas phase*, in Designing ceramic interfaces II: Understanding and tailoring interfaces for coating, composite and joining applications; Proceedings of the Second European Colloquium, Petten, 11–13 November 1993, edited by Stathis D. Peteves (Office for Official Publications of the European Communities, Luxembourg, 1992).
[110] This approximation is all the more reasonable as the particles are close to their equilibrium shape (see Sec. V C).